J. Fluid Mech. (2006), *vol.* 564, *pp.* 105–138.
doi:10.1017/S0022112006001352 Printed in the United Kingdom

Surfactant-induced fingering phenomena beyond the critical micelle concentration

By B. D. EDMONSTONE[1], R. V. CRASTER[2] AND O. K. MATAR[1]†

[1]Department of Chemical Engineering and Chemical Technology, Imperial College London, South Kensington, London, SW7 2AZ, UK

[2]Department of Mathematics, Imperial College London, South Kensington, London SW7 2AZ, UK

(Received 1 August 2005 and in revised form 6 February 2006)

We consider the spreading of a droplet of soluble surfactant, at concentrations beyond its critical micelle concentration (CMC), on a pre-existing thin liquid layer. Lubrication theory is used to derive a coupled system of four two-dimensional nonlinear evolution equations for the film thickness and surfactant concentration at the interface and in the bulk as both monomers and micelles. These equations are parameterized by a number of dimensionless groups that reflect the relative importance of Marangoni stresses, surface and bulk diffusion, capillarity, surfactant solubility, sorption kinetics and the nonlinearity of the equation of state. Our results for the base state indicate that two parameters in particular exert a significant influence on the flow profiles: the dimensionless mass of surfactant deposited, M, and a parameter reflecting the preference of the surfactant to form micelles, R. For a fixed value of R, increasing M leads to the development of a protuberance that appears at the edge of the drop; upon increasing M further, this protuberance separates from the drop to form a distinct secondary front that lies behind a leading front that usually accompanies the spreading process. Our examination of the linear and nonlinear stability of the system through a transient growth analysis and transient numerical simulations, respectively, indicates that these features are vulnerable to transverse perturbations, leading to the formation of fingers. The results obtained in the present work are in qualitative agreement with recently available experimental data.

1. Introduction

The spreading of surfactant-laden fluid droplets over thin pre-existing fluid layers or solid substrates has received considerable attention in both the theoretical and experimental literature (see the recent review by Afsar-Siddiqui, Luckham & Matar 2003*a* and references therein). The mechanisms behind spreading and wetting are critical to applications in a range of diverse settings that span coating flows, agrochemicals and drug delivery. The addition of a surface-active material (a surfactant) can have a dramatic effect on the spreading properties of a liquid droplet (Stoebe *et al.* 1997*a, b*). In many of these settings, such as manufacturing chemical sprays, for instance, the increased spreading rates that result from surfactant addition are desirable. For processes in which this beneficial effect should be optimized, a full understanding of the surfactant's role is required.

† Author to whom correspondence should be addressed: o.matar@imperial.ac.uk

The spreading process for surfactant monolayers over thin fluid layers, in the absence of perturbations, is well-understood for both soluble and insoluble surfactants (see, for instance, Jensen & Grotberg 1992, 1993; Afsar-Siddiqui *et al.* 2003*a* and references therein). The increase in the rates of spreading is related to the presence of surfactant concentration gradients, which give rise to surface tension gradients and, in turn, to Marangoni stresses that lead to spreading in the direction of low concentrations (high surface tension). These stresses deform the underlying liquid film so that a thickened fluid ridge forms at the surfactant leading edge with a severely thinned region appearing upstream of the ridge, near the surfactant deposition. Experimental observations, however, have revealed that surfactant-driven spreading is often accompanied by the formation of fingering patterns that appear, with varying intensity and structure, behind the advancing front. These fingering phenomena (see examples shown in figure 1) have been observed by a number of research groups using a variety of different surfactants on solid substrates pre-wetted with thin films of varying thickness (Marmur & Lelah 1981; Troian, Wu & Safran 1989*b*; He & Ketterson 1995; Frank & Garoff 1995; Bardon *et al.* 1996; Cachile *et al.* 1999; Cachile & Cazabat 1999; Fischer, Darhuber & Troian 2001; Cachile *et al.* 2002; Afsar-Siddiqui, Luckham & Matar 2003*a, b*; Darhuber & Troian 2003; Hamraoui *et al.* 2004). This fingering instability affects the efficiency of the spreading process and the surface coverage achieved.

The need to isolate the physical mechanism responsible for these fingering phenomena has motivated a number of modelling studies, beginning with the work of Troian, Herbolzheimer & Safran (1990) who considered the spreading of a thick drop, laden with insoluble surfactant, on a thinner liquid film. Their linear stability analysis revealed that Marangoni stresses are responsible for the instability. This work exploited certain similarities between the surfactant-driven fingering phenomena and the well-known viscous fingering problem. Matar & Troian (1999) and Warner, Craster & Matar (2002) conducted a transient growth analysis and full numerical simulations of the spreading of a surfactant monolayer (rather than a surfactant-laden drop) on a thin film of initially uniform thickness. This analysis showed that considerable transient perturbation growth, ultimately followed by decay and not localized in the thinning region, can occur in the absence of van der Waals forces, which, when included, gave rise to asymptotic growth in the thinning region. Fischer & Troian (2003) showed that it is possible to obtain sustained perturbation growth, for the monolayer problem, in the absence of van der Waals forces but only in the presence of continuous 'feeding' of surfactant at the flow origin.

More recently, Warner, Craster & Matar (2004*a, b*) examined the flow of a thick surfactant deposition on a much thinner film (with negligible van der Waals forces) using linear stability and transient growth analyses, together with numerical simulations, and showed that the fingering mechanism is intimately linked to the adverse mobility gradients in the thinning region; these gradients owe their existence to the large disparity in thickness between the deposited drop and the thinner underlying film, pre-wetting the solid substrate. The thickness disparity introduced in the model is the vital ingredient missing in earlier models of the fingering process; asymptotic methods (Jensen & Naire 2006) can be used to explore the origin of the fingering mechanism further. Increasing the ratio of the 'precursor' thickness to that of the drop led to a decrease in growth and eventually to decay of applied perturbations. Full numerical simulations of the nonlinear governing equations showed the evolution of fingering patterns in the thinned region that bear great resemblance to those observed experimentally. Incidentally, surfactant-induced Marangoni stresses have

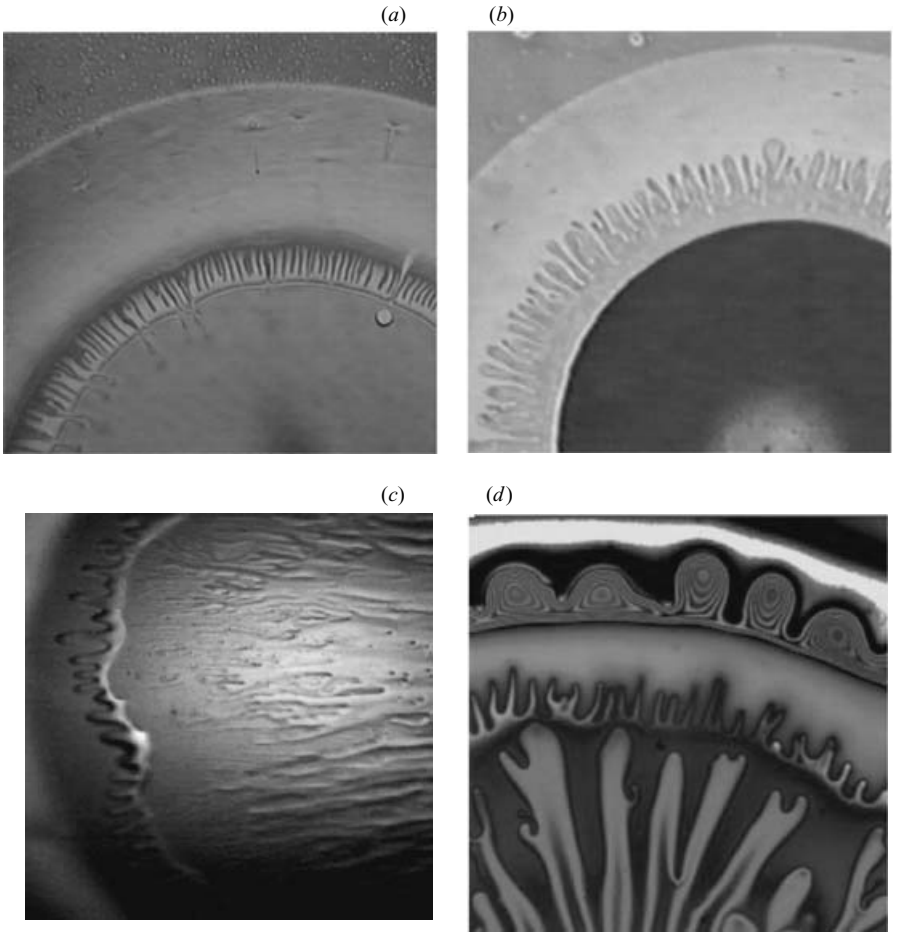

FIGURE 1. Four typical experimental photographs: (*a*) and (*b*) are reprinted from Hamraoui *et al.* 2004 (with permission from Elsevier) ((*a*) $C_{12}E_{10}$ at 1.5 CMC on a 120 nm film of ethyleneglycol (EG), (*b*) $C_{12}E_4$ at 1 CMC on a 120 nm EG film); (*c*) by Luckham and co-workers (2.8 CMC SDS in a 4:1 glycerol/water suspension on an approximately 250 nm film) and (*d*) reprinted from Darhuber & Troian (2003) with permission (SDS in glycerol spreading on a 1–10 μm film). (*a*) The fingers are situated in the thinned region between the drop and the thickened front; this the case that has been successfully modelled by Warner *et al.* (2004*a*, *b*). (*b*) The fingers protrude from the foot of the drop, in the absence of a pronounced thickness minimum. (*c*) The elevated region (to the left of the photograph) that exhibits fingers is actually upstream of an advancing front that is barely visible as the light ring in the photograph (L. Lee, M. Gee & P. F. Luckham personal communication, 2005); this provides evidence for the emergence of two fronts. Note that the region upstream of the fingered front also exhibits fingers, which are more ramified and resemble streamlets. Panel (*d*) A thickened front at the top develops ahead of the thinned region which appears to exhibit instabilities on two different scales.

recently also been shown to further destabilize the flow of a thin film down an inclined plane (Edmonstone, Matar & Craster 2005) in which a fingering instability occurs in the surfactant-free case.

The modelling work on the fingering instability, however, has focused on the case of dilute surfactant concentrations, well below the critical micelle concentration

(CMC). Yet the majority of the experimental studies have considered situations in which the concentration exceeds the CMC (Troian *et al.* 1989; Cachile *et al.* 2002; Afsar-Siddiqui *et al.* 2003*a, b*; Hamraoui *et al.* 2004). The importance of the CMC is that surfactants are typically amphiphilic, that is, containing components that are hydrophobic and hydrophillic. An amphiphilic molecule can arrange itself in different ways to achieve equilibrium, the preferred state being at the interface, with the polar group in the aqueous medium and the non-polar part held above the surface; this is the preferred arrangement at concentrations below the CMC. However, beyond the CMC the molecules rapidly form aggregates, micelles, in the bulk in which the hydrophobic tails are oriented within the micelle and the hydrophilic polar head groups are in contact with the (aqueous) solvent.

The most recent experimental work of Cazabat and co-workers (Hamraoui *et al.* 2004) has demonstrated the emergence of some important features of the flow, which are simply not captured by the existing models for surfactant droplet spreading. For instance, the surfactant-driven thickened rim in the experiments often advances in time like $t^{1/2}$, consistent with reservoir feeding of surfactant, rather than $t^{1/4}$ which is the power-law predicted by our existing models that is consistent with the deposition of a finite mass of surfactant (Jensen & Grotberg 1992); clearly there is a discrepancy. This indicates the existence of a mechanism, absent from our models, that gives rise to behaviour that mimics that associated with the spreading of a front being supplied from an infinite reservoir of surfactant. The minimum in the film thickness which, in all of the studies in the literature, appears near the surfactant deposition, upstream from the advancing rim is only present in the work of Hamraoui *et al.* (2004) for concentrations above the (CMC) or for spreading over solid substrates pre-coated with sufficiently thick films (in excess of 100 nm) (see figure 1*a*). These researchers have shown that the minimum is completely absent from the thickness profiles in the case of spreading over very thin films or bare solid substrates, and for dilute concentrations. Yet in spite of its absence, Hamraoui *et al.* (2004) have still observed fingering; in these cases, the fingers appear to grow almost directly out from the side of the drop (see figure 1*b*). These are important points: first, our models for the base state always predict the presence of a minimal thickness; second, this feature of the flow, according to Warner *et al.* (2004*a, b*), controls the onset and evolution of the fingering patterns. Hamraoui *et al.* (2004) have also shown that the degree of finger branching exhibits a maximum for a surfactant concentration for which the rate of change of the surface tension with respect to the surface concentration is maximal, indicating the necessity of having a sufficiently large flux from the surfactant deposition to provide feeding of the fingers from the upstream end. Moreover, recent work using the surfactant sodiumdodesylsulphate (SDS) in either glycerol or glycerol/water suspensions (Darhuber & Troian 2003; L. Lee, M. Gee & P. F. Luckham, Personal Communication, 2005) shows the development of two thinning regions with associated fingered spreading (see figure 1*c, d*). It is also clear from figure 1(*c*) that the inner set of fingers undergoes considerable tip-splitting and exhibits fractal-like patterns, which bear great resemblance to those generated via diffusion-limited aggregation or Laplacian-driven processes. The outer set of fingers is, in contrast, much less ramified. There is no existing theory that captures or explains this two-thinned-regions phenomenon.

The recent experimental observations mentioned above and shown in figure 1 pose new challenges and questions to which predictive models of the surfactant spreading problem should provide answers. This article provides answers to some of these questions via detailed modelling of the spreading of thick drops laden with soluble

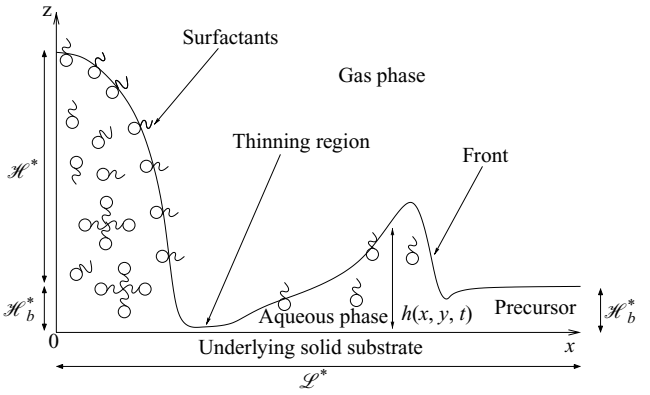

FIGURE 2. A schematic of the typical flow geometry. A surfactant-laden drop containing both micelles and monomers is deposited upon a clean pre-existing film. The surface tension variation drives the flow that creates a leading front and a thinned region separating it and the drop.

surfactant, present at concentrations that can exceed the CMC, on thin liquid films of varying thickness. Lubrication theory will be used to develop evolution equations for the film thickness and the surfactant concentration, which will be present in the form of monomers (that have a bulk and an interfacial concentration) and micelles. The derivation of these equations builds on that of Breward & Howell (2004), who studied the effect of micellar formation on a flow in a different context. Rapid vertical diffusion of surfactant in the bulk is assumed (Jensen & Grotberg 1993; Warner *et al.* 2004*b*) so that vertical concentration variations are erased over very short time scales, allowing the dynamics of the concentrations to be described by one-dimensional partial differential equations. The model accounts for Marangoni stresses, capillarity, surface and bulk diffusion, and the formation and breakup of micelles; closure is achieved by a nonlinear surfactant equation of state.

The rest of this paper is organized as follows. In § 2 the governing equations will be developed, along with the initial and boundary conditions. Section 3 will deal with the dynamics of the unperturbed spreading process and the effect of each parameter on the evolution of the model. Section 4 will present results of a stability analysis, including the results from the fully nonlinear two-dimensional simulations. Section 5 will provide some discussion and concluding remarks.

2. Formulation

2.1. *Governing equations*

We consider the dynamics of a drop of an incompressible, Newtonian fluid with viscosity μ^* and density ρ^* laden with soluble surfactant, which has been deposited on a rigid and impermeable solid substrate, pre-wetted with an uncontaminated thin uniform fluid film of the same fluid as the drop (figure 2). This mimics the experiments by Hamraoui *et al.* (2004) and others, which involve careful preparation of a thin fluid layer upon which the surfactant-laden droplet is then placed. The initial thicknesses of the drop and pre-existing film are $\mathscr{H}^*$ and $\mathscr{H}_b^*$ respectively. The geometric ratio, b, defined as $b \equiv \mathscr{H}_b^*/\mathscr{H}^*$ characterizes the disparity in thickness between the droplet and the underlying fluid layer. The characteristic width of the drop is $\mathscr{L}^*$ and is

assumed to greatly exceed $\mathscr{H}^*$ so that the drop aspect ratio, $\epsilon \equiv \mathscr{H}^*/\mathscr{L}^*$, is assumed to be very small, which permits the use of lubrication theory; this will be used below to derive the evolution equations that govern the system dynamics.

Here we allow the concentration of the surfactant in the drop to exceed the critical micelle concentration (CMC) beyond which the surfactant can be present in three different forms: as a monomer, which can exist either in the bulk or at the interface with concentrations c^* and Γ^*, respectively, or as a micellar aggregate with concentration m^*. The exchange between the different phases proceeds as follows. First at the interface

$$\Gamma' \rightleftharpoons S + c', \tag{2.1}$$

which represents the transfer of a surface molecule, Γ', into the bulk phase, c', thus creating a space, S, at the free surface or conversely a monomer from the bulk using up a space at the interface; this model leads, at equilibrium, to the Langmuir isotherm and accounts for the effect, important at high concentrations, that the interfacial surfactant monomer may fully pack the interface. Implicit in the model is that the total space at the interface is limited, i.e. in terms of the concentrations $\Gamma^* + s\Gamma^*_\infty = \Gamma^*_\infty$, with Γ^*_∞ as the concentration at maximum packing. Secondly, the micelles and bulk monomer are related via

$$n\ c' \rightleftharpoons m', \tag{2.2}$$

which represents the creation of a micelle, m', in the bulk phase from n free bulk surfactant molecules, or the breakup of a micelle into n bulk monomers.

These relations carry with them certain implicit and natural assumptions. For instance, it is assumed that the micelles do not adsorb directly onto the interface, but that they must completely disassociate first into bulk monomers. It is also assumed that there is a strongly preferred micelle size, n, which is indeed often the case in reality (Hunter 1991).

This is a considerable idealization of micelle disassociation which is in itself a complex process. The simple one-step model used here is about the simplest available which captures the essence of an aggregate of monomers breaking up and reforming. This area remains an active one: a recent review by Noskov (2002) summarizes micellization kinetics and their influence upon surfactant adsorption and one can utilize more complicated polydisperse and multiple step models that model the breakup process more realistically, see also Hunter (1991). Alternatively, other simple disassociation models such as, say, the Fainerman model used in Liao, Basaran & Franses (2003) could be utilized at this point in the analysis; we return to this in our concluding remarks.

We shall also assume that the initial concentration of each of these phases is uniform within the droplet and that equilibrium conditions prevail.

We use a rectilinear coordinate system, (x^*, y^*, z^*), to model the dynamics in which x^*, y^* and z^* denote the horizontal, transverse and vertical coordinates and the velocity field is $\boldsymbol{u}^* = (u^*, v^*, w^*)$ and u^*, v^* and w^* correspond to the components of the velocity field in these directions, respectively. The free surface and solid substrate are located at $z^* = h^*(x^*, y^*, t^*)$ and $z^* = 0$, respectively, where t^* represents time. Marangoni spreading is driven by the spreading pressure $\mathscr{S}^* = \sigma^*_c - \sigma^*_m$, which is the difference between the surface tension of the initial surfactant deposition, σ^*_m, and that of the underlying clean uncontaminated film, σ^*_c. The local surface tension, σ^*, is dependent on the local value of the surfactant surface concentration, Γ^*, through the so-called Sheludko equation of state (Sheludko 1967; Gaver & Grotberg 1990)

which is nonlinear and appropriate for use at high surfactant concentrations:

$$\frac{\sigma^*}{\mathscr{S}^*} = (\alpha+1)\left(1+\frac{\Gamma^*}{\Gamma^*_\infty}\left[((\alpha+1)/\alpha)^{1/3}-1\right]\right)^{-3}, \tag{2.3}$$

in which $\alpha \equiv \sigma^*_m/\mathscr{S}^*$. Here, Γ^*_∞ represents the interfacial surfactant concentration at maximum packing. Inspection of (2.3) reveals that, at high concentrations, Marangoni stresses are not only dependent on the gradient Γ^*_x, but also on the concentration Γ^*. Other equations of state are available, and in use, (see, for instance, Edwards, Brenner & Wasan 1991 and references therein); we choose the Sheludko model for definiteness. It is not thermodynamically consistent with the Langmuir isotherm used later (Chang & Frances 1995), however we simply use it as an empirical model with an easily adjustable nonlinearity.

The spreading dynamics are governed by the equations of continuity and the Navier–Stokes equations:

$$\nabla\cdot\boldsymbol{u}^* = 0, \qquad \rho^*(\boldsymbol{u}^*_{t^*} + \boldsymbol{u}^*\cdot\nabla\boldsymbol{u}^*) = -\nabla p^* + \mu^*\nabla^2\boldsymbol{u}^*, \tag{2.4}$$

where p^* is the pressure and we have neglected gravitational and intermolecular forces. Convective–diffusion equations for the concentration of the surfactant phases are taken as

$$\Gamma^*_{t^*} + \nabla_s\cdot(\boldsymbol{u}^*_s\Gamma^*) + \Gamma^*(\boldsymbol{u}^*\cdot\boldsymbol{n}^*)\kappa^* = D^*_s\nabla^2\Gamma^* + J^*_{\Gamma c}, \tag{2.5}$$

$$c^*_{t^*} + \boldsymbol{u}^*\cdot\nabla c^* = D^*_b\nabla^2 c^* - nJ^*_{cm}, \tag{2.6}$$

$$m^*_{t^*} + \boldsymbol{u}^*\cdot\nabla m^* = D^*_m\nabla^2 m^* + J^*_{cm}. \tag{2.7}$$

Here, Γ^*, c^* are the concentrations of surface and bulk monomers and m^* is the concentration of micelles; each micelle contains n monomers; the subscript 's' signifies interfacial quantities, $D_i (i = b, m, s)$ represent the diffusion coefficients (assumed to be constant) of the monomers in the bulk, the micelles, and of the monomers at the surface, respectively; k^*_1 and k^*_2 are adsorption and desorption rate constants associated with monomer transport to and from the interface, and k^*_3 and k^*_4 are the rate constants associated with the formation, and breakup, of micellar aggregates of n surfactant monomer molecules. In (2.5), $\kappa^* = \nabla_s\cdot\boldsymbol{n}$ is the curvature of the fluid surface in which $\nabla_s = (\boldsymbol{I}-\boldsymbol{nn})\cdot\nabla$ wherein $\boldsymbol{n} = \nabla h^*/|\nabla h^*|$ is the outward pointing normal to the interface and $\boldsymbol{I}$ is the identity tensor.

Equations (2.5)–(2.7) are complemented by the sorptive flux relations governing the exchange of monomer species between the surface and bulk:

$$J^*_{\Gamma c} = k^*_1 c^*_s\left(1-\frac{\Gamma^*}{\Gamma^*_\infty}\right) - k^*_2\Gamma^*, \tag{2.8}$$

which follows from (2.1) and notably contains a nonlinear term such that when $\Gamma^* \to \Gamma^*_\infty$, that is, when the surface becomes fully packed with monomers, no further surfactant is adsorbed. At equilibrium, this is the Langmuir adsorption isotherm and for dilute concentrations, when this nonlinear term is absent, the linearized sorption kinetics model used by Jensen & Grotberg (1993) is obtained. Other isotherms (see, for instance, Chang & Frances 1995) are available to model different kinetics, but the Langmuir model is widely adopted and incorporates the surface packing behaviour and so it is used here.

Similarly, there is a sorptive flux controlling the exchange between monomers and micelles in the bulk:

$$J^*_{cm} = k^*_3 c^{*n} - k^*_4 m^*. \tag{2.9}$$

Notably, the law of mass action when applied to (2.2) leads to the nonlinear term in c^*; for large values of n, which are typical of micelles, this can lead to sharp changes in the micelle concentration.

Solutions of (2.4) are obtained subject to no-slip and no-penetration conditions, $\boldsymbol{u}^* = 0$, at $z^* = 0$, in addition to continuity of the normal and tangential stresses, and the kinematic boundary condition at $z^* = h^*(x^*, y^*, t^*)$, respectively given by

$$\boldsymbol{n} \cdot \boldsymbol{T}^* \cdot \boldsymbol{n} = \sigma^* \kappa^*, \tag{2.10}$$

$$\boldsymbol{n} \cdot \boldsymbol{T}^* \cdot \boldsymbol{t} = \boldsymbol{t} \cdot \nabla_s \sigma^*, \tag{2.11}$$

$$h^*_{t^*} + u^*_s h^*_{x^*} = w^*, \tag{2.12}$$

where $\boldsymbol{T}^* = -p^* + \mu^*(\nabla \boldsymbol{u}^* + \nabla \boldsymbol{u}^{*\mathrm{T}})$ is the total stress tensor and $\mathbf{t}$ is the tangent to the interface. The boundary conditions imposed on the variables to be determined from (2.5)–(2.7) are that

$$(\Gamma^*_{x^*}, c^*_{x^*}, m^*_{x^*}) = 0 \qquad \text{at} \quad x^* = (0, L^*_x), \tag{2.13}$$

$$\left.\begin{aligned} -D^*_b[\boldsymbol{n}^* \cdot \nabla c^*]_s = J^*_{\Gamma c}, \qquad m^*_{z^*} = 0 \qquad \text{at} \quad z^* = h^*(x^*, y^*, t^*), \\ (c^*_{z^*}, m^*_{z^*}) = 0 \qquad \text{at} \quad z^* = 0, \end{aligned}\right\} \tag{2.14}$$

where L^*_x is the dimensional length of the spatial domain in the horizontal direction; periodic boundary conditions are imposed on all variables in the transverse direction. The only boundary condition worthy of comment is $m^*_z = 0$ at $z^* = h^*$ which implies that no micelles are adsorbed directly to the surface, but must break up into bulk monomers first.

The total mass of surfactant deposited per unit width, M^*, is

$$\int_0^\infty \int_0^{h^*} (c^* + n m^*)\, \mathrm{d}z^* \mathrm{d}x^* + \int_0^\infty \Gamma^* \mathrm{d}x^* = M^*, \tag{2.15}$$

which is conserved. The scalings adopted in the present work are presented next.

2.2. *Scaling*

The governing equations, sorptive fluxes and boundary conditions are rendered dimensionless via the following scalings:

$$\left.\begin{aligned} &(x^*, y^*, z^*, h^*) = \mathscr{L}^*(x, y, \epsilon z, \epsilon h), \quad (u^*, v^*, w^*) = \mathscr{U}^*(u, v, \epsilon w), \quad t^* = \frac{\mathscr{L}^*}{\mathscr{U}^*} t, \\ &p^* = \frac{\mathscr{S}^*}{\mathscr{H}^*} p, \quad \Gamma^* = \Gamma^*_\infty \Gamma, \quad c^* = c^*_{cmc} c, \quad m^* = \left(\frac{c^*_{cmc}}{n}\right) m, \quad \sigma^* = \mathscr{S}^* \sigma + \sigma^*_m, \\ &J^*_{\Gamma c} = \left(\frac{\mathscr{U}^* \Gamma^*_\infty}{\mathscr{L}^*}\right) J_{\Gamma c}, \quad J^*_{cm} = \left(\frac{\mathscr{U}^* c^*_{cmc}}{\mathscr{L}^*}\right) J_{cm}, \end{aligned}\right\} \tag{2.16}$$

where $\mathscr{U}^* = \mathscr{S}^* \mathscr{H}^* / (\mu^* \mathscr{L}^*)$ and $c^*_{cmc} = (k^*_4 / n k^*_3)^{1/(n-1)}$. The characteristic bulk surfactant concentration has been taken to be the critical micelle concentration c^*_{cmc}, and when non-dimensionalizing the micelle concentration we have inserted a factor of n so the non-dimensional micelle concentration is a measure of the concentration of monomers present in the micellar phase.

Substitution of (2.16) into (2.4)–(2.14), yields the following two-dimensional set of coupled, highly nonlinear evolution equations for h, Γ, c and m in the lubrication

approximation ($\epsilon \to 0$) (Edmonstone 2005):

$$h_t = -\nabla\cdot\left(\frac{\mathscr{C}}{3}h^3\nabla\nabla^2 h + \frac{1}{2}h^2\nabla\sigma\right), \tag{2.17}$$

$$\Gamma_t = \frac{\nabla^2\Gamma}{Pe_s} - \nabla\cdot\left(\frac{\mathscr{C}}{2}h^2\Gamma\nabla\nabla^2 h + h\Gamma\nabla\sigma\right) + J_{\Gamma c}, \tag{2.18}$$

$$c_t = \frac{1}{hPe_b}\nabla\cdot(h\nabla c) - \left(\frac{\mathscr{C}}{3}h^2\nabla\nabla^2 h + \frac{h}{2}\nabla\sigma\right)\cdot\nabla c - \frac{\beta}{h}J_{\Gamma c} - J_{cm}, \tag{2.19}$$

$$m_t = \frac{1}{hPe_m}\nabla\cdot(h\nabla m) - \left(\frac{\mathscr{C}}{3}h^2\nabla\nabla^2 h + \frac{h}{2}\nabla\sigma\right)\cdot\nabla m + J_{cm}, \tag{2.20}$$

where $\sigma = [(\alpha+1)/\alpha](1+\theta(\alpha)\Gamma)^{-3} - \alpha$ in which $\theta(\alpha) = (\alpha+1))^{1/3} - 1$ and the fluxes $J_{\Gamma c}$ and J_{cm} are expressed by

$$J_{\Gamma c} = K_s(Rc(1-\Gamma) - \Gamma), \tag{2.21}$$

$$J_{cm} = K_b(c^n - m). \tag{2.22}$$

Note that we have invoked the rapid vertical diffusion assumption in deriving (2.19) and (2.20) by substituting

$$(c, m)(x, y, z, t) = (c_0, m_0)(x, y, t) + \epsilon^2(Pe_b, Pe_m)(c_1, m_1)(x, y, z, t), \tag{2.23}$$

into these equations, taking the limit $\epsilon^2(Pe_b, Pe_m) \to 0$ and performing cross-sectional averaging; note that $(1/h)\int_0^h (c_1, m_1)\mathrm{d}z = 0$ (Jensen & Grotberg 1993; Warner *et al.* 2004*b*; Edmonstone 2005) and that the '0' subscripts have been suppressed. The dimensionless surfactant monomer mass deposited per unit width is

$$\int_0^\infty h(c+m)\,\mathrm{d}x + \beta\int_0^\infty \Gamma\,\mathrm{d}x = M, \tag{2.24}$$

where M^* has been non-dimensionalized with $H^*\mathscr{L}^* c^*_{cmc}$, i.e. the volume times the critical micelle concentration.

This is a parametrically rich problem. The dimensionless groups that appear in (2.17)–(2.22) are $\mathscr{C} \equiv \epsilon^2\sigma^*_m/\mathscr{S}^*$, a capillary parameter, $Pe_i \equiv (\mathscr{U}^*\mathscr{L}^*/D^*_i)(i = b, m, s)$ are Péclet numbers representing a ratio of convective to diffusive time scales for the monomers and micelles in the bulk and the monomers at the interface, respectively; $\beta \equiv \Gamma^*_\infty/(\mathscr{H}^* c^*_{cmc})$ provides a dimensionless measure of the degree of solubility of the surfactant into the bulk solute ($\beta \ll 1$ signifies high solubility and $\beta \gg 1$ is a virtually insoluble surfactant trapped upon the surface); $(K_s, K_b) \equiv (k^*_2, k^*_4)\mathscr{L}^*/\mathscr{U}^*$ are dimensionless kinetics constants, giving a time scale for local equilibrium to occur between the phases; $R \equiv k^*_1 c^*_{cmc}/(k^*_2\Gamma^*_\infty)$ is a dimensionless measure of the ease with which micelles are formed within the bulk. Thus for small R values one would expect the majority of the surfactant to exist in the bulk, either in monomer or micellar form; conversely, for large R, the surfactant interfacial concentration is expected to be large.

In addition we have a parameter, α, that gives a measure of the nonlinearity of the equation of state; large α corresponds to a linear equation of state. The dimensionless mass of surfactant present, M, is also an important parameter in the model as a dilute approximation is no longer valid. There is also a parameter, b, giving a measure of height difference between the thin film and the drop: small b corresponds to a large droplet placed upon a very thin fluid layer; our earlier work shows that this parameter is important for finger formation. Indeed, in Warner *et al.* (2004*a*), it is shown that

System parameter	Representation	Value range
Capillary parameter	$\mathscr{C} \equiv \epsilon^2 \sigma_m^* / \mathscr{S}^*$	0.1–0.0001
Surface Péclet number	$Pe_s \equiv \mathscr{U}^* \mathscr{L}^* / D_s^*$	100–100,000
Bulk monomer Péclet number	$Pe_b \equiv \mathscr{U}^* \mathscr{L}^* / D_b^*$	10–10,000
Micelle Péclet number	$Pe_m \equiv \mathscr{U}^* \mathscr{L}^* / D_m^*$	10–10,000
Surfactant solubility	$\beta \equiv \Gamma^* / \mathscr{H} c_{cmc}^*$	0.01–∞
Surface kinetics parameter	$K_s \equiv k_2^* \mathscr{L}^* / \mathscr{U}^*$	0.1–100
Bulk kinetics parameter	$K_b \equiv k_4^* \mathscr{L}^* / \mathscr{U}^*$	0.1–100
Surfactant distribution parameter	$R \equiv k_1^* c_{cmc}^* / k_2^* \Gamma_\infty^*$	0.01–100
Equation of state parameter	$\alpha \equiv \sigma_m^* / \mathscr{S}^*$	0.1–∞
Preferred micelle size	n	5–100
Surfactant mass	$M = \mathscr{H}^* c_{cmc}^* \mathscr{L}^*$	0.1–20
Thickness ratio: film/drop height	$b = \mathscr{H}_b^* / \mathscr{H}^*$	0–1

TABLE 1. Definitions and order of magnitude estimates of the dimensionless parameters appearing in (2.17)–(2.22).

increasing b eventually leads to a situation where the spreading process is stable and one reverts to a surfactant monolayer spreading problem: in the numerical simulations we choose a value of b intended to be typical of that in experiments where a relatively large droplet is placed upon a pre-existing thin film of fluid (of the order of 100 nm thick).

Estimates of these dimensionless parameters are found in table 1 with parameter ranges obtained from a number of sources that have examined surfactant-driven flows (Chang & Frances 1995; Jensen & Grotberg 1993; Afsar-Siddiqui *et al.* 2003*a, b*; Warner *et al.* 2004*a, b*).

2.3. *Linearization and growth measures*

In order to investigate the stability of the spreading process to infinitesimally small transverse perturbations, we insert the decomposition

$$(h, \Gamma, c, m)(x, y, t) = (h_0, \Gamma_0, c_0, m_0)(x, t) + (h_1, \Gamma_1, c_1, m_1)(x, t) \exp(\mathrm{i}ky), \tag{2.25}$$

into (2.17)–(2.22) and linearize the resultant equations about the nonlinear base state h_0, Γ_0, c_0 and m_0. Here, the subscripts '0' and '1' respectively denote one-dimensional base-state variables and disturbance quantities, characterized by a wavenumber k. The nonlinear base-state equations are

$$h_{0t} = -\left[\frac{\mathscr{C}}{3} h_0^3 h_{0xxx} + \frac{1}{2} h_0^2 \sigma_{0x}\right]_x, \tag{2.26}$$

$$\Gamma_{0t} = \frac{\Gamma_{0xx}}{Pe_s} - \left[\frac{\mathscr{C}}{2} h_0^2 \Gamma_0 h_{0xxx} + h_0 \Gamma_0 \sigma_{0x}\right]_x + K_s(Rc_0(1-\Gamma_0) - \Gamma_0), \tag{2.27}$$

$$c_{0t} = \frac{(h_0 c_{0x})_x}{Pe_b h_0} - \frac{\mathscr{C}}{3} h_0^2 c_{0x} \kappa_{0x} - \frac{1}{2} h_0 \sigma_{0x} c_{0x} - \frac{\beta K_s}{h_0}(Rc_0(1-\Gamma_0) - \Gamma_0) - K_b\left(c_0^n - m_0\right), \tag{2.28}$$

$$m_{0t} = \frac{(h_0 m_{0x})_x}{Pe_m h_0} - \frac{\mathscr{C}}{3} h_0^2 m_{0x} \kappa_{0x} - \frac{1}{2} h_0 \sigma_{0x} m_{0x} + K_b\left(c_0^n - m_0\right), \tag{2.29}$$

with $\kappa_0 = h_{0xx}$.

The evolution equations governing the dynamics of the linear perturbations are given by

$$h_{1t} = -\frac{\mathscr{C}}{3}\left[\left(h_0^3\kappa_{1x} + 3h_0^2h_1\kappa_{0x}\right)_x - k^2h_0^3\kappa_1\right] - \frac{1}{2}\left[\left(h_0^2\sigma_{1x} + 2h_0h_1\sigma_{0x}\right)_x - k^2h_0^2\sigma_1\right], \quad (2.30)$$

$$\begin{aligned}\Gamma_{1t} = &-\frac{\mathscr{C}}{2}\left[\left(h_0^2\Gamma_0\kappa_{1x} + h_0^2\Gamma_1\kappa_{0x} + 2h_0h_1\Gamma_0\kappa_{0x}\right)_x - k^2h_0^2\Gamma_0\kappa_1\right]\\ &- \left[(h_0\Gamma_0\sigma_{1x} + h_0\Gamma_1\sigma_{0x} + h_1\Gamma_0\sigma_{0x})_x - k^2h_0\Gamma_0\sigma_1\right] + \frac{1}{Pe_s}(\Gamma_{1xx} - k^2\Gamma_1)\\ &+ K_s(R(c_1 - c_1\Gamma_0 - c_0\Gamma_1) - \Gamma_1), \end{aligned} \quad (2.31)$$

$$\begin{aligned}c_{1t} = &-\frac{\mathscr{C}}{3}\left[h_0^2c_{0x}\kappa_{1x} + h_0^2c_{1x}\kappa_{0x} + 2h_0h_1c_{0x}\kappa_{0x}\right] - \frac{1}{2}[h_0\sigma_{0x}c_{1x} + h_0\sigma_{1x}c_{0x} + h_1\sigma_{0x}c_{0x}]\\ &+ \frac{1}{Pe_b}\left[\frac{1}{h_0}(h_{0x}c_{1x} + h_{1x}c_{0x}) - \frac{h_{0x}c_{0x}h_1}{h_0^2} + c_{1xx} - k^2c_1\right] - \frac{\beta K_s}{h_0}(R(c_1 - c_1\Gamma_0 - c_0\Gamma_1)\\ &- \Gamma_1) + \beta K_s\frac{h_1}{h_0^2}\left(Rc_0(1-\Gamma_0) - \Gamma_0\right) - K_b(nc_1c_0^{n-1} - m_1), \end{aligned} \quad (2.32)$$

$$\begin{aligned}m_{1t} = &-\frac{\mathscr{C}}{3}\left[h_0^2m_{0x}\kappa_{1x} + h_0^2m_{1x}\kappa_{0x} + 2h_0h_1m_{0x}\kappa_{0x}\right] - \frac{1}{2}[h_0\sigma_{0x}m_{1x} + h_0\sigma_{1x}m_{0x} + h_1\sigma_{0x}m_{0x}]\\ &+ \frac{1}{Pe_m}\left[\frac{1}{h_0}(h_{0x}m_{1x} + h_{1x}m_{0x}) - \frac{h_{0x}m_{0x}h_1}{h_0^2} + m_{1xx} - k^2m_1\right]\\ &- K_b(nc_1c_0^{n-1} - m_1). \end{aligned} \quad (2.33)$$

Since the base state evolves in both space and time, we use the following definition for the asymptotic growth rate of a perturbation, $\omega_i (i = h, \Gamma, c, m)$ (Edmonstone *et al.* 2005):

$$\omega_i = \lim_{t\to\infty}\frac{\ln \mathscr{G}_i(t)}{2t}, \qquad i = h, \Gamma, c, m, \quad (2.34)$$

where $\mathscr{G}_i$ are amplification ratios given by

$$\mathscr{G}_i(t) = \frac{(E_{i_1}/E_{i_0})(t)}{(E_{i_1}/E_{i_0})(t=0)}, \qquad i = h, \Gamma, c, m. \quad (2.35)$$

Here, $E_q(t) = \int_0^\infty (q - q_\infty)^2(x,t)\,\mathrm{d}x$ where $(q = h_0, h_1, \Gamma_0, \Gamma_1, c_0, c_1, m_0, m_1)$ and $(q_\infty = b, 0, 0, 0, 0, 0, 0, 0)$. In §4 we use these to create numerical 'dispersion curves' that illustrate the dependence of ω_h on k and capture the 'linear stability' characteristics of the spreading process as a function of system parameters.

2.4. *Numerical procedure*

The numerical scheme EPDCOL (Sincovec & Madsen 1979; Keast & Muir 1991) is used to obtain solutions of the one-dimensional evolution equations. This reliable scheme, which uses finite element collocation for spatial discretization and Gear's method in time, has previously been used to solve equations governing surfactant-driven thin films accurately and efficiently (Warner *et al.* 2004*a*, *b*); 2000–3000 grid points were used in the majority of the computations over the spatial interval $0 \leqslant x \leqslant L_x = 30$.

The initial condition used for the film thickness is given by

$$h_0(x,0) = (1 + b - x^2)F(1-x) + b\ F(x-1), \quad (2.36)$$

$$(\Gamma_0, c_0, m_0)(x,0) = (\Gamma_o, c_o, m_o)F(1-x), \quad (2.37)$$

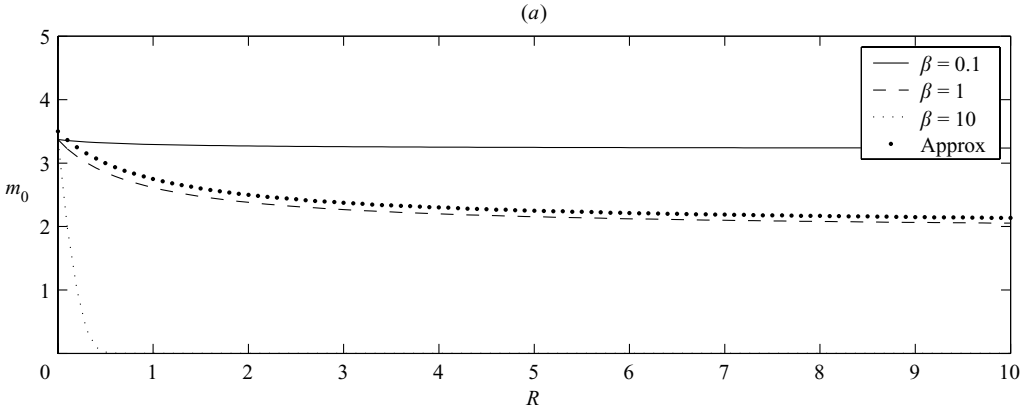

FIGURE 3. Variation of the initial micelle concentration, m_0, with R for $\beta = 0.1, 1, 10$. Also shown as the thin dotted line is an approximate relation for m_o given by (2.40); here, $M = 3$ and $n = 10$.

where $F(x) = \frac{1}{2}[1 + \tanh(100x)]$. In order to relate the values of (Γ_o, c_o, m_o) to the mass of surfactant deposited, we assume that, at $t = 0$, the fluxes $J_{\Gamma c} = J_{cm} = 0$ so the surfactant is in local equilibrium initially, whence

$$c_o = m_o^{1/n}, \qquad \Gamma_o = \frac{R m_o^{1/n}}{1 + R m_o^{1/n}}. \tag{2.38}$$

Substitution of (2.38) into (2.24) and ignoring the precursor layer yields

$$\frac{2}{3}\left(m_o^{1/n} + m_o\right) + \frac{\beta R m_o^{1/n}}{1 + R m_o^{1/n}} = M, \tag{2.39}$$

which is solved numerically for m_o (> 0) for a prescribed value of M(see figure 3).

If we assume that $n \gg 1$, so that $m_o^{1/n} \approx 1$, then simple formulae for Γ_o, c_o and m_o emerge as

$$\Gamma_o \sim \frac{R}{1+R}, \qquad c_o \sim 1, \qquad m_o \sim \frac{3}{2}\left(M - \frac{\beta R}{1+R}\right) - 1. \tag{2.40}$$

For $R \ll 1$, we then have

$$\Gamma_o \sim 0, \qquad c_o \sim 1, \qquad m_o \sim \frac{3M}{2} - 1, \tag{2.41}$$

while for $R \gg 1$ we have

$$\Gamma_o \sim 1, \qquad c_o \sim 1, \qquad m_o \sim \frac{3}{2}(M - \beta) - 1. \tag{2.42}$$

For $M \gg 1$, we have

$$\Gamma_o \sim \frac{R}{1+R}, \qquad c_o \sim 1, \qquad m_o \sim \frac{3M}{2}, \tag{2.43}$$

suggesting that increasing the total mass of deposited surfactant simply results in a significant increase in the initial concentration of micelles and a relatively minor change in the surface and bulk concentrations of the monomers. Also, for $\beta \ll 1$, the

limit of high solubility, we have

$$\Gamma_o \sim \frac{R}{1+R}, \qquad c_o \sim 1, \qquad m_o \sim \frac{3M}{2} - 1, \tag{2.44}$$

while in the insoluble surfactant limit, $\beta \gg 1$,

$$\Gamma_o \sim 1, \qquad c_o \sim 0, \qquad m_o \sim 0; \tag{2.45}$$

hence all the surfactant is present at the interface.

If $M \leqslant 1$ then we begin to enter the dilute regime where micelles are not present, and indeed solving (2.39) numerically gives $m_o \ll 1$. Here the natural variable is c_o and one sets $m_o = 0$ (and decouples the m_0 equation from consideration). The initial concentrations are found by solving

$$\frac{2}{3}c_o + \frac{\beta R c_o}{1+Rc_o} = M, \quad \Gamma_o = \frac{Rc_o}{1+Rc_o}. \tag{2.46}$$

The solutions obtained for $(h_0, \Gamma_0, c_0, m_0)(x, t)$ are subject to the following boundary conditions:

$$h_{0x} = h_{0xxx} = \Gamma_{0x} = c_{0x} = m_{0x} = 0 \quad \text{at} \quad x = (0, L_x), \tag{2.47}$$

where the L_x denotes the dimensionless length of the computational domain in the x-direction.

The initial conditions for the perturbations represent disturbances localized near the flow origin:

$$h_1(x, 0) = \Gamma_1(x, 0) = c_1(x, 0) = m_1(x, 0) = 0.005 \exp(-5x^2), \tag{2.48}$$

while the boundary conditions are chosen to preserve undisturbed conditions far away from the drop and to impose symmetrical solutions about the flow origin:

$$h_{1x} = h_{1xxx} = \Gamma_{1x} = c_{1x} = m_{1x} = 0 \quad \text{at} \quad x = (0, L_x). \tag{2.49}$$

In order to obtain numerical solutions of the two-dimensional evolution equations, (2.17)–(2.22), the procedure used by Warner, *et al.* (2004*a*, *b*) is utilized in the present work. This is based on an alternating-direction-implicit (ADI) scheme (see also Witelski & Bowen 2003), which employs operator splitting methods enabling computations to be carried out via solution of one-dimensional problems that results in considerable increase in efficiency. Two-dimensional numerical solutions are obtained starting from

$$\left.\begin{aligned} h(x, y, 0) &= (1 - x^2 + b)F(1-x) + bF(x-1) + Af(x, y), \\ (\Gamma, c, m)(x, y, 0) &= (\Gamma_o, c_o, m_o)F(1-x), \end{aligned}\right\} \tag{2.50}$$

where the amplitude $A \in (10^{-3} - 10^{-2})$ and $f(x, y)$ are pseudo-random perturbations to the film thickness, the perturbations having a uniform distribution on $[-0.01, 0.01]$, which is an initial condition more representative of an experiment. Alternatively one chooses $f(x, y) = \exp(-\mathrm{B}x^2) \sum_{i=1}^{N} C_i \cos(q_i y)$ for some constants B, q_i, N so that this is a finite-amplitude perturbation consisting of several transverse modes localized at the edge of the surfactant deposition.

The transient numerical simulations of (2.17)–(2.20) are performed on a grid $0 < x < L_x$, $0 < y < L_y$ and are subject to the following boundary conditions:

$$\left.\begin{aligned} (h_x, h_{xxx})(0, y, t) &= 0, \qquad h(L_x, y, t) = b, \quad h_x(L_x, y, t) = 0, \\ (\Gamma_x, c_x, m_x)(0, y, t) &= 0, \qquad (\Gamma, c, m)(L_x, y, t) = 0, \end{aligned}\right\} \tag{2.51}$$

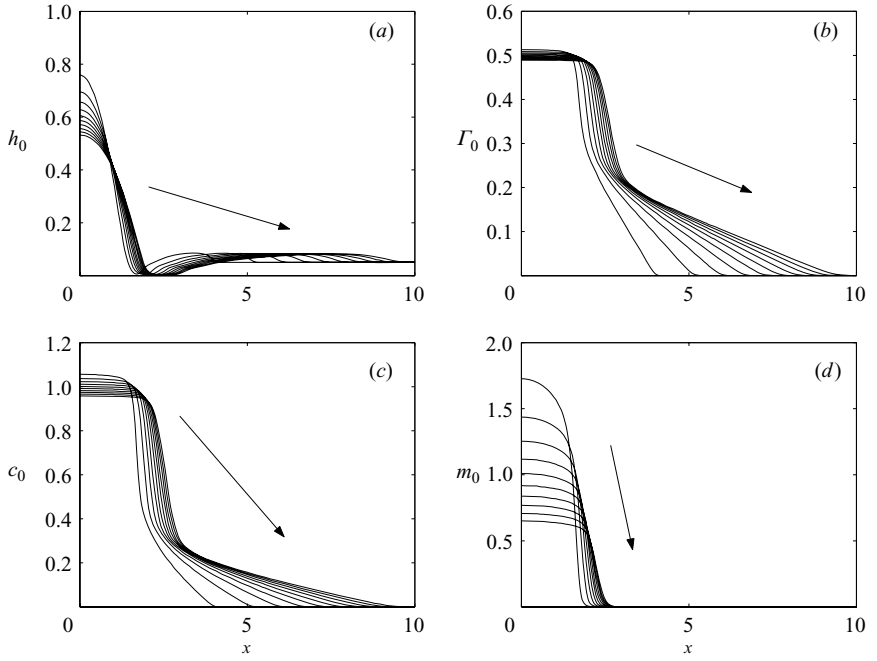

FIGURE 4. Spatio-temporal evolution of h_0, Γ_0, c_0 and m_0, shown in (*a–d*), respectively, generated for the 'base' case (see text in § 2.4), except that $R = 1$, for $t = 0$ to 1000 with the profiles drawn at intervals of 100. Here, the arrows indicate the direction of increasing time.

where L_y is the dimensionless transverse length of the computational domain. Periodic boundary conditions are imposed along the edges of the grid along $y = (0, L_y)$. Typically we utilize a 2π square grid and have a 200×200 mesh. We have ensured that the results obtained from the transient growth analysis are reproduced by the ADI scheme starting from small-amplitude perturbations. This comparative study made use of the following definition for the 'energy' of the film thickness perturbation:

$$E_{h_1} = \frac{k}{\pi} \int_{-\pi/k}^{\pi/k} \int_{0}^{\infty} [h(x, y, t) - h_0(x, t)]^2 \, \mathrm{d}x \, \mathrm{d}y, \tag{2.52}$$

with similar definitions introduced for the remaining variables.

Numerical solutions were obtained over a wide range of parameters. The 'base' case, however, has broadly typical values of $\mathscr{C} = 10^{-3}$, $Pe_s = 10^4$, $Pe_b = Pe_m = 10^2$, $K_s = 1$, $K_b = 1$, $\beta = 1$, $R = 10$, $\alpha = 100$, $n = 10$, $M = 3$, $b = 0.05$ and $t = 10^4$. Since the effect of capillarity, surface and bulk diffusion, and sorption kinetics, characterized by $\mathscr{C}$, Pe_s, α and Pe_b, and K_s, respectively, have been investigated by Jensen & Grotberg (1992, 1993), Warner *et al.* (2004*a*, *b*) and others, we concentrate mainly on the effect of varying M, R, Pe_m, K_b and n on the dynamics. The numerical results for the base state are presented next.

3. Base state

We begin the discussion of our results by showing in figure 4 a typical evolution of the base-state variables, h_0, Γ_0, c_0 and m_0 generated with the 'base' parameter set,

except $R = 1$. For these values of M and R, $\Gamma_o = 0.524$, $c_o = 1.101$ and $m_o = 2.613$ which imply that a significant proportion of the surfactant is initially in the form of micellar aggregates. Inspection of figure 4(*a*) reveals that the drop spreads gradually under the action of the Marangoni stresses in the direction of lower concentrations. A thickened front is formed at the surfactant leading edge, which has thickness approximately equal to $2b$, and propagates rapidly relative to the drop; severe thinning occurs in the region between the drop and the front. The drop, which must spread over this much thinner region downstream, remains as a cap at late times. The behaviour of the leading front is apparently similar to that for monolayer spreading (Jensen & Grotberg 1992, 1993) and the 'trapping' of the droplet and the development of the severely thinned region is similar to that found for insoluble and soluble surfactant droplet deposition by Warner *et al.* (2004*a*, *b*). Several of the observed features, for instance the shock-like behaviour in the height field at the surfactant leading edge, are characterized by small-scale features with large slope that might render lubrication theory invalid; however as time progresses the width of the shock increases and the slopes become more moderate (Jensen & Grotberg 1992) and hence one expects the results here to be valid except for very small times.

The Γ_0 and c_0 profiles, shown in figure 4(*b*, *c*) exhibit three regions of interest: a region of almost uniform concentration near the flow origin, followed downstream by two regions of approximately constant concentration gradient; the latter regions coincide with the thinning region and the elevated region upstream of the ridge in the film thickness profile. The concentration of micelles, m_0, decreases significantly with time, as shown in figure 4(*d*). It is also evident that the micelles are spatially localized near the origin (m_0 eventually becomes zero-valued in the thinning region) and appear to remain completely trapped within the drop for the duration of the spreading process. The drop, therefore, acts like a source of micelles, which, in turn, dissociate into monomers, on time scales of order $1/K_b$, that exist in the bulk or at the interface depending on the relative magnitude of K_s and R. It is worth noting that the local surfactant concentrations come rapidly into a local quasi-equilibrium so $c_0 \sim m_0^{1/n}$ and $\Gamma_0 \sim Rc_0/(1 + Rc_0)$. This is observed numerically, and one can construct a single surfactant evolution equation on that basis; however it is unwieldy. This quasi-equilibrium where $m_o \sim c_o^n$ ensures, for large n, that the micelles only exist where $c_o \sim 1$ (i.e. within the droplet) and rapidly disassociate for $c_o < 1$.

We now present the results of our parametric study of the base state. In figure 5, we show the effect of varying the total mass of surfactant ($M = 1, 3, 5$) deposited on the flow characteristics for high values of R ($R = 100$); we recall that high values of R imply a relatively high threshold for the formation of micelles and a preference for the surfactant to be at the interface. In this case the micelles within the drop act as a reservoir of surfactant that, in turn, acts as an 'insoluble' surfactant; once released it is drawn inexorably to the surface. Increasing M results in a significant rise in the concentration of micelles in the drop region and a retention of large gradients in c and Γ to relatively late times. These, in turn, give rise to large Marangoni stresses that increase the thickness of the advancing ridge and lead to severe thinning upstream; the latter effect leads to 'pinning' of the drop which maintains a relatively large height till late times.

A very notable feature appears in the height and surfactant profiles: as the surfactant mass increases, the interface in the thinned region develops, for $M = 3$, a distinct protuberance from the droplet edge. This feature resembles the thickened advancing capillary ridge in gravity-driven thin film flow down an inclined plane (Troian *et al.* 1989*a*) and thermally driven climbing films (Kataoka & Troian 1997).

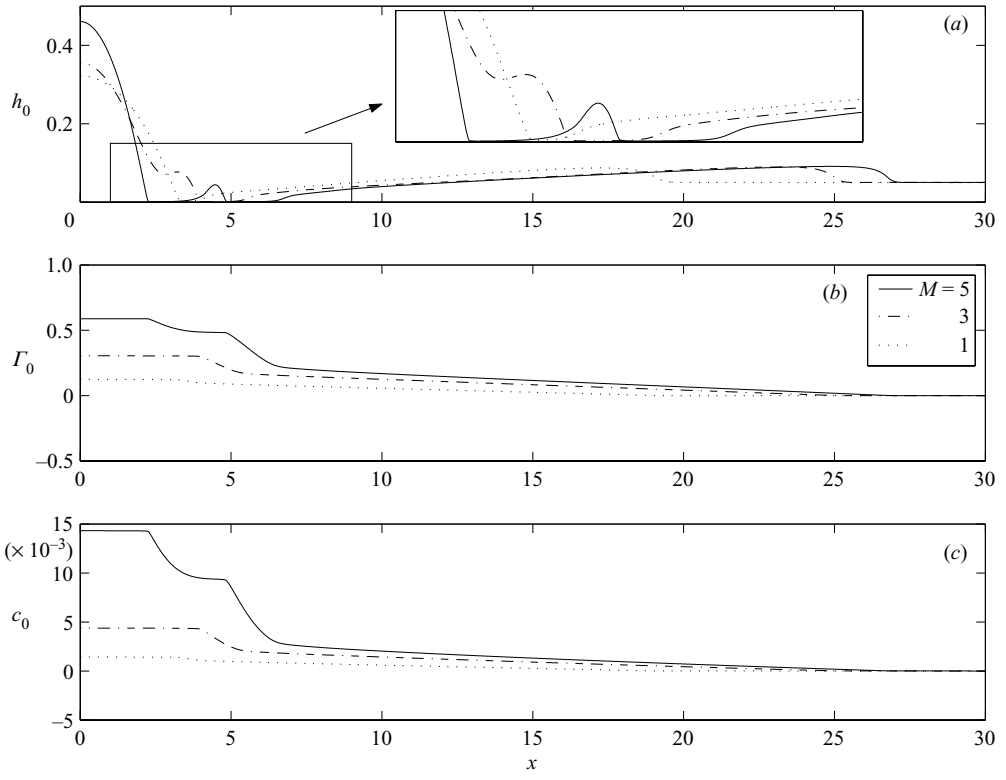

FIGURE 5. The effect of varying the dimensionless mass, M, on h_0, Γ_0 and c_0, with $M = 1, 3, 5$, $R = 100$ and $t = 10^4$; the remaining parameters are unaltered from figure 4. The m_0 profiles are not shown since m_0 is approximately zero-valued at $t = 10^4$ for this set of parameters.

More remarkably, for $M = 5$, this splits away from the main drop to form an isolated front, henceforth termed the 'secondary' front, separated from both the leading front and the main droplet by severely thinned regions; this is shown in detail in the inset of figure 5(*a*). These may appear to be ruptured regions or 'dry spots' as viewed by an experimental observer; indeed these regions may be so thin that intermolecular forces could be operational within them. The appearance of the secondary front is reminiscent of that observed in the experiments of Lee *et al.* (personal communication, 2005) shown in figure 1(*c*). The surfactant is virtually all in the interfacial phase and, interestingly, the Γ_0 profile associated with $M = 5$ no longer exhibits three constant-gradient regions like those associated with $M = 1$ and $M = 3$ (or the $M = 3$ and $R = 1$ case shown in figure 4), but develops a somewhat extended, rather flat, region upstream of the secondary front. The magnitude of the bulk surfactant, c_0, is extremely small, the reservoir of micelles is exhausted by $t = 10^4$, and they are completely absent (hence they are not shown in figure 5).

It is clearly of interest to understand how the protuberance and secondary front are formed. To elucidate this, we inspect the early time behaviour, shown in figure 6, which depicts h_0 and Γ_0 for two cases: $M = 5$, for which the secondary front forms, and $M = 1$, for which it does not. For relatively early times, $0 \leqslant t \leqslant 10$, it becomes clear that a small 'lip' is beginning to form at the edge of the droplet (see figure 6*a*); at later times (shown in figure 5*a*), this develops into the secondary front. This lip is absent from the $M = 1$ case (see figure 6*b*): here the whole droplet begins to move at

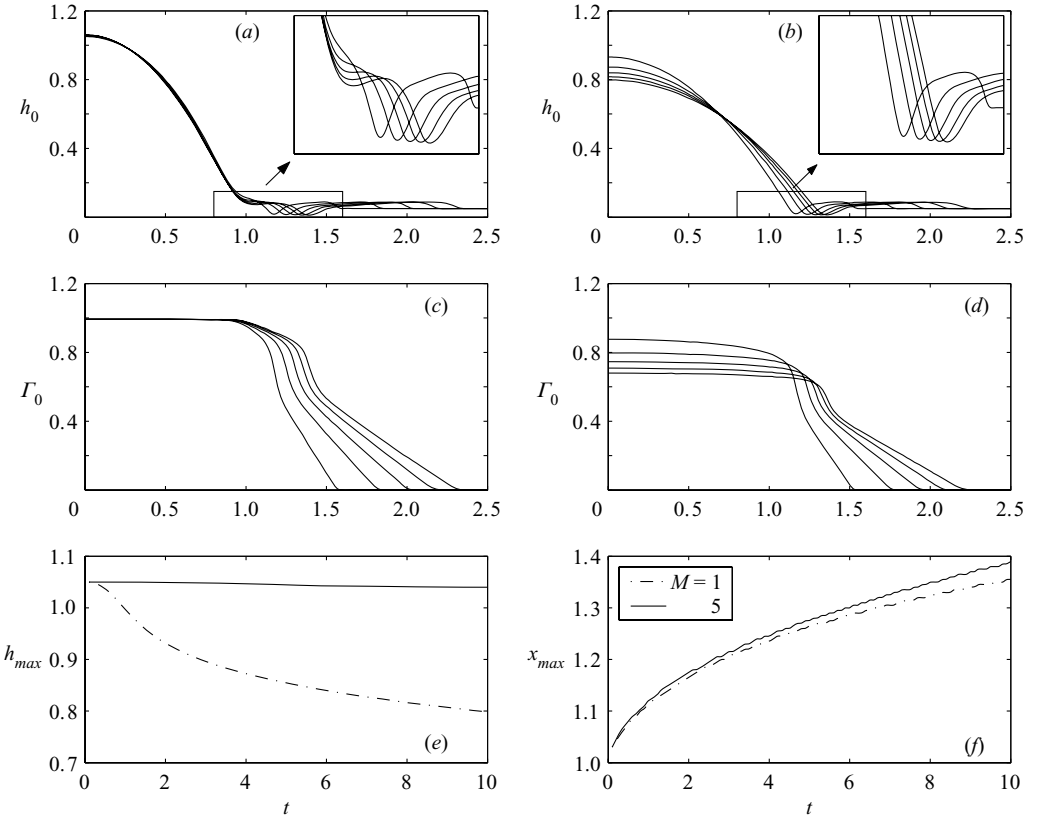

FIGURE 6. The early time development of the 'secondary' front: (*a*) and (*c*) show the height, h_0, and interfacial surfactant, Γ_0, development for $t = 1, 2, \ldots 10$ for the base parameter set with $M = 5$ and $R = 100$. (*b*) and (*d*) The same variables, but for $M = 1$. The lines are at $t = 2, 4, 6, 8, 10$. The maximal height and position of the height minimum are shown in (*e*) and (*f*), respectively, with $M = 5$ (solid lines) and $M = 1$ (dashed lines).

time $t = 0$. The surface surfactant is drawn into the uncontaminated region with the low bulk and micelle concentrations unable to replenish the surface concentration. This forms a concentration gradient, and hence surface tension driving force, across the whole droplet. The droplet profile for $M = 5$, when contrasted with that for $M = 1$, seems to suffer very little structural variation (see figure 6*a*), except very close to the droplet edge. In this case, the surfactant is able to replenish itself at the interface from the higher bulk and micelle concentrations that exist. Only the fluid at the edge of the deposition is affected by the Marangoni-generated flow and change in surface surfactant concentration. In the region from $x = 0$ to $x = 0.75$ the situation is almost static with only the capillary forces attempting to deform the droplet. At the edge of the deposition, however, a surface tension gradient forms and flow is generated, drawing fluid out in the new elongated shape that is seen in many of the numerical results. This is clearly seen via inspection of the Γ_0 profiles: for $M = 5$, Γ_0 is continually replenished from the micelle 'reservoir' so that $\Gamma_0 \approx 1$ within the droplet region and Γ_{0_x} is strongly localized at the droplet edge which acts to push the lip out (see figure 6*c*). For $M = 1$, $\Gamma_0(0, t)$ and $h_0(0, t)$ decrease, the whole droplet is deformed outwards and a pronounced lip is absent (although x_{min}, the position of the minimal height, appears to be weakly dependent on M, as shown in figure 6*f*).

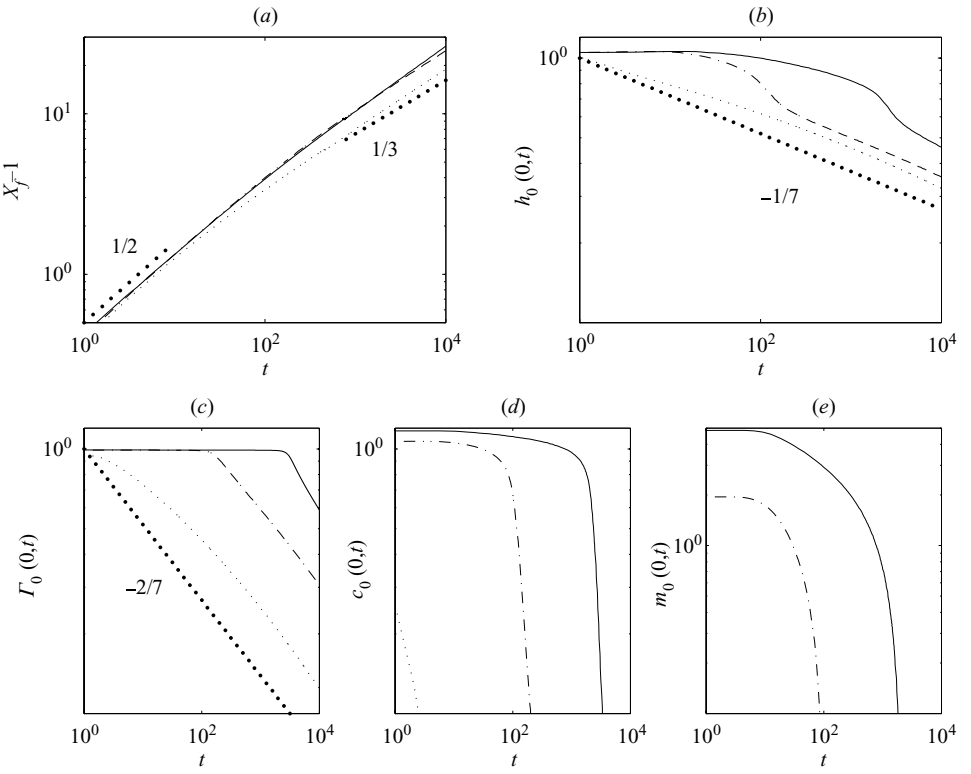

FIGURE 7. Temporal evolution of the leading front position relative to the edge of the original droplet deposition, $X_f - 1$, (*a*), the height of the droplet at the origin $h_0(0, t)$, (*b*), and the surfactant concentrations at the origin $\Gamma_0(0, t)$, $c_0(0, t)$ and $m_0(0, t)$ (*c–e*), respectively, out to $t = 10^4$. The parameter values are the same as in figure 5. The thick dotted lines in (*a–c*) have constant slopes equal to $1/2$, $-1/7$ and $-2/7$, respectively.

This is because at the higher M values, the relative abundance of micelles in the droplet region sustains the development of large concentration gradients, which are, in principle, capable of giving rise to several advancing fronts. We conjecture that the reason that only two fronts are observed is the thinning which occurs upstream of the primary front, which hinders severely the progress of the secondary front and prevents the formation of others.

It is also instructive to consider the complementary results shown in figure 7, in which we show the temporal evolution of several quantities of interest. In figure 7(*a*), we plot the position of the leading front, X_f, relative to initial droplet edge. During the early stages of the spreading process, $X_f - 1 \sim t^{1/2}$ which corresponds to the scaling for a reservoir-fed monolayer (Jensen & Grotberg 1992) and to the scaling observed in the experiments by Hamraoui *et al.* (2004) and at early times in the modelling work of Starov, de Ryck & Velarde (1997). At later times, the front position appears to modify its behaviour to $t^{1/3}$ which, when re-interpreted in axisymmetry, is that of monolayer spreading of a constant surfactant mass as observed in the studies of Starov, de Ryck & Velarde (1997) and Afsar-Siddiqui *et al.* (2003*a*, *b*). In figure 7(*b–e*), we plot the temporal evolution of $(h_0, \Gamma_0, c_0, m_0)(0, t)$, respectively. It is seen clearly that the micelles act as a reservoir, dynamically feeding the monolayer bulk and interface concentrations (see figure 7*e*). However, following an initial transient (whose

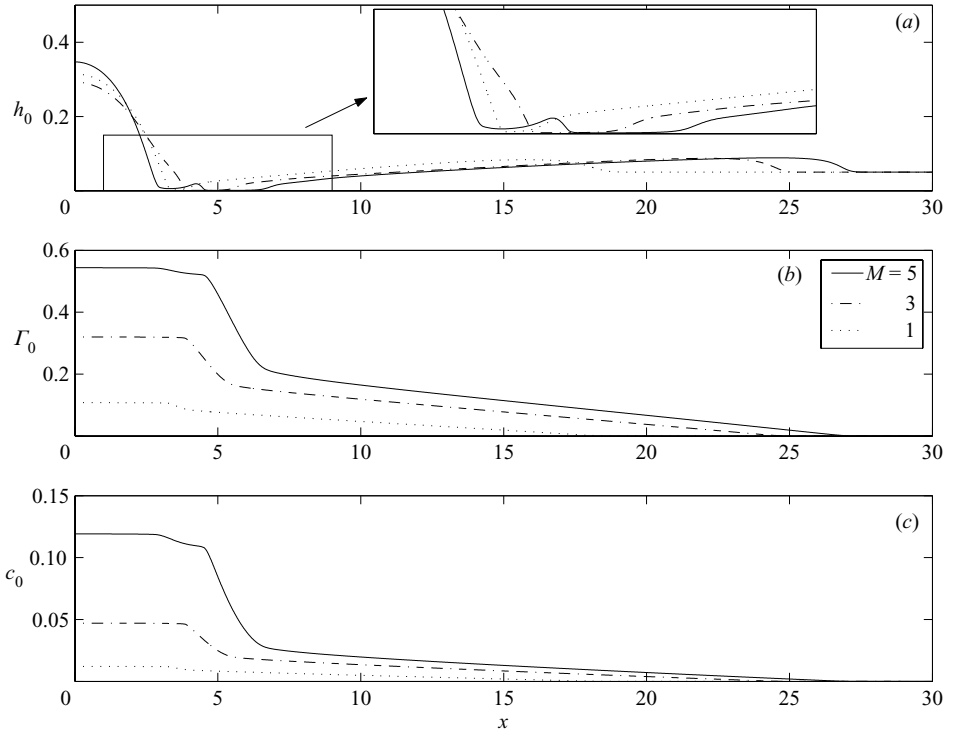

FIGURE 8. The effect of varying the dimensionless mass, M, on h_0, Γ_0 and c_0, with $M = 1, 3, 5$, $R = 10$ and $t = 10^4$; the remaining parameters are the same as in figure 4.

period increases with M for a fixed value of R) that coincides approximately with the stage of the spreading process during which $X_f - 1 \sim t^{1/2}$, the supply of micelles is exhausted and the scalings $h_0(0, t) \sim t^{-1/7}$ (Jensen & Naire 2006) and $\Gamma_0(0, t) \sim t^{-2/7}$ are recovered; these are associated with the spreading of an insoluble surfactant droplet on a thinner substrate for dilute concentrations.

Next, we examine the effect of altering R on the flow profiles. As R is decreased from $R = 100$ to $R = 10$ (see figure 8) and then to $R = 1$ (see figure 9), the amplitude of the secondary front decreases. Also, the micelles, whose 'preference' to remain in the bulk of the droplet until the latter stages of spreading increases with decreasing R (see figure 9*d*), act as reservoir for longer (they are still present in the bulk after 10^4 time units, as shown in figure 9*d*). Thus decreasing the value of R, which corresponds to a relatively low threshold for micelle formation, gives rise to a marked increase in the magnitude of m_0 and c_0, as expected (one now has a reservoir release of 'soluble' surfactant rather than one which, for $R = 100$, has a strong affinity to the interface). The gradients in Γ_0 (c_0 and m_0) and therefore the magnitude of the Marangoni stresses become smaller (larger) with decreasing (increasing) R, leading to a slower spreading process, which is characterized by a weak front and a shallower thinning region. Indeed, inspection of the temporal evolution of the front location versus times in figure 10 reveals that it does not achieve the $t^{1/3}$ scaling although the drop itself does appear, particularly for $M = 1$, to move towards the known scalings of $h_0(0, t) \sim t^{-1/7}$ and, importantly, for the surfactant $\Gamma_0(0, t) = c(0, t) \sim t^{-2/7}$. These scalings are formally valid for an insoluble surfactant droplet and so the lack of agreement is, perhaps, not so surprising. In the limit of small R one moves towards

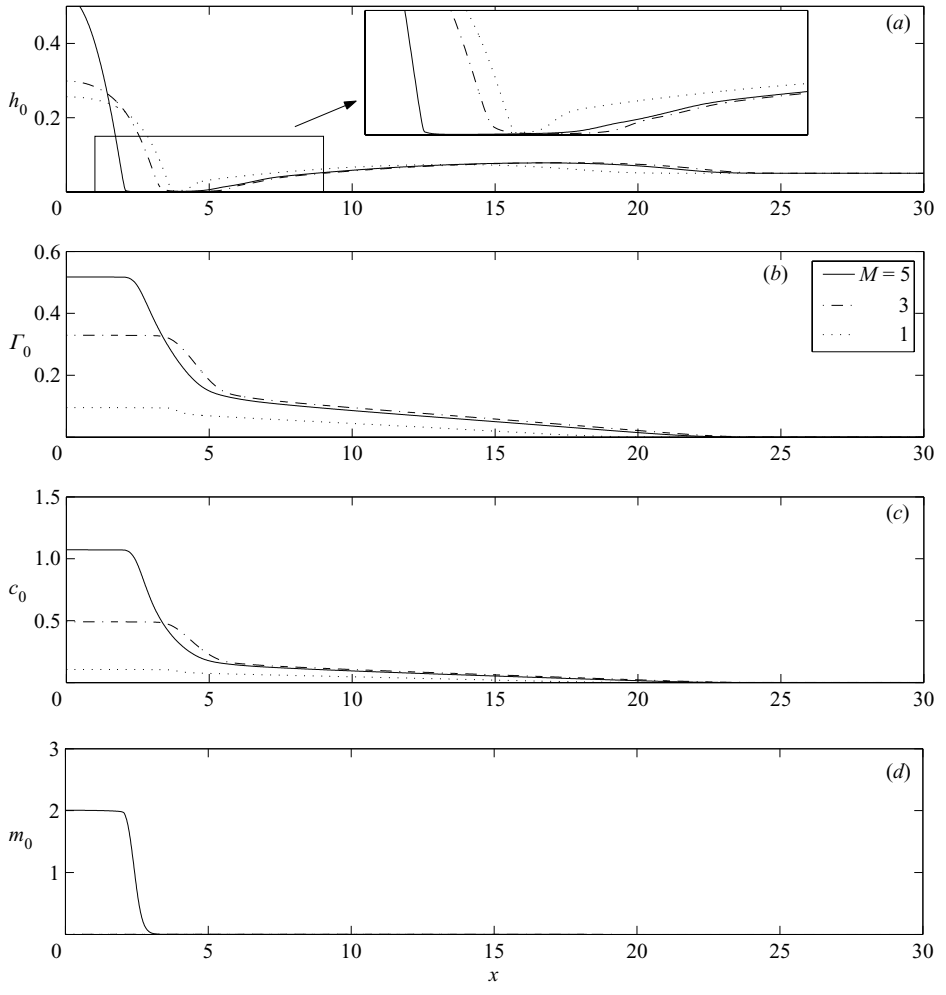

FIGURE 9. The effect of varying the dimensionless mass, M, on h_0, Γ_0, c_0 and m_0, with $M = 1, 3, 5$, $R = 1$ and $t = 10^4$; the remaining parameters are unaltered from figure 4.

a situation where the bulk surfactant monomer and interfacial surfactant both play an important role and the height profiles in figure 9 resemble those in Warner *et al.* (2004*b*) that exhibit a smaller amplitude front at the leading edge.

The foregoing discussion has focused on the effect of varying M and R on the dynamics. We illustrate in figure 11 the effect of n, Pe_s, $Pe_{b,m}$, b and α on the h_0 profiles. As shown in figure 11(*a*), increasing the micelle size acts to confine the micelles even more strongly within the drop. This is because the flux J_{cm} is proportional to $c_0^n - m_0$ and high powers of n act to 'cut off' the micelle concentration outside the drop; the effect is to steepen the drop and increase the amplitude of the secondary front. Decreasing the surface Péclet number, Pe, which promotes surface diffusion of the surfactant molecules, leads to faster spreading and acts to move the locations of the secondary and leading fronts further downstream; this is shown in figure 11*b*. For $Pe = 10$ the profiles do not exhibit front formation. Increasing both the bulk and micelle Peclet numbers, $Pe_{b,m}$, which reduces bulk diffusion of these species, has the effect of depressing the droplet and suppressing the formation of the secondary

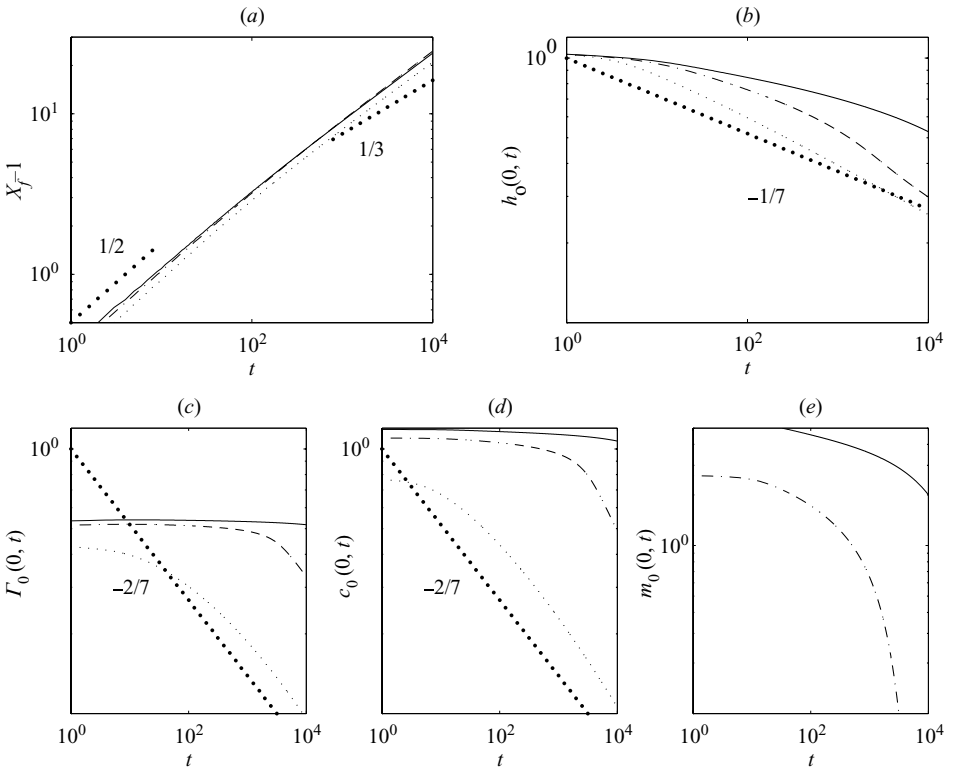

FIGURE 10. Temporal evolution of the leading front position relative to the edge of the original droplet deposition, $X_f - 1$, (*a*), the height of the droplet at the origin $h_0(0,t)$, (*b*), and the surfactant concentrations at the origin $\Gamma_0(0,t)$, $c_0(0,t)$ and $m_0(0,t)$, (*c–e*), respectively, out to $t = 10^4$. The parameter values are the same as in figure 5. The thick dotted lines in (*a–c*) have constant slopes equal to $1/2$ and $1/3$, $-1/7$ and $-2/7$, respectively.

front (see figure 11*c*) although the results associated with $Pe_{b,m} = 1000$ should be interpreted with caution since such large values may render the rapid vertical diffusion assumption, $\epsilon^2 Pe_{b,m} \ll 1$, invalid. For increasing b, we see that the surfactant leading front travels much further and the thinning is less pronounced, as expected (see figure 11*d*). Variations in this geometric parameter are examined in the earlier insoluble surfactant model by Warner *et al.* (2004*b*), and eventually, for b sufficiently large there is a small droplet upon a relatively thick pre-existing film and a return to a monolayer spreading problem as in Jensen & Grotberg (1992). One can approach a similar limiting case in this micellar model: although some care is required with the initial conditions. We have also found that decreasing the value of α, which increases the degree of nonlinearity of the nonlinear equation of state, leads to an increase in h_0 at the origin, the retention of large gradients in m_0, c_0 and Γ_0 (not shown) to relatively late times, and the formation of wide 'dry spots' between the primary and secondary fronts (whose height diminishes with decreasing α) and elevated ridges downstream.

The effect of altering the remaining parameters on the flow profiles has been discussed in previous studies (Warner *et al.* 2004*b*), hence only a brief summary of this effect is provided here. Other results (not shown) indicate that promoting solubility through a reduction of β increases the concentration of micelles in the bulk of the deposited drop, which, in turn, act as monomer sources, leading to a substantial increase

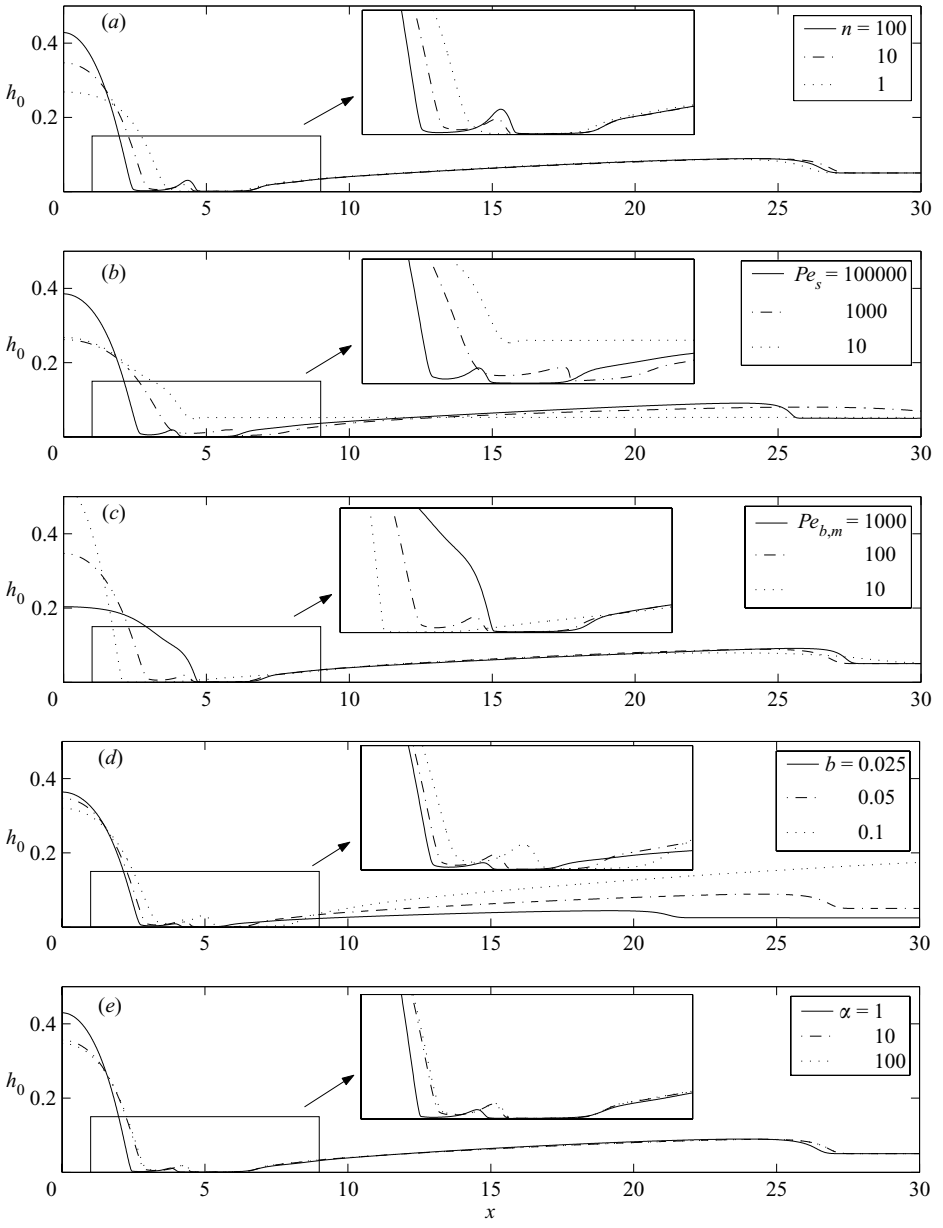

FIGURE 11. The effect of varying n, Pe_s, $Pe_{b,m}$, b and α on h_0, shown in (a–e), respectively, at $t = 10^4$. The parameters are the same as in figure 8 and $M = 5$.

in the gradients of Γ_0 and c_0. Consequently, the film thickness profiles associated with low β values exhibit a wide, thickened advancing ridge preceded by a severely thinned region, which is attached to a large drop near the flow origin. The parameter K_b represents a ratio of the flow time scale to that associated with the breakup of micelles; thus, large (small) K_b values signify rapid (slow) micelle dissociation. Increasing K_b leads to a substantial increase in m_0 near the flow origin and a concomitant increase in both c_0 and Γ_0. The resulting increase in the magnitude of the concentration gradients and the Marangoni stresses give rise to more severe thinning and the formation of a

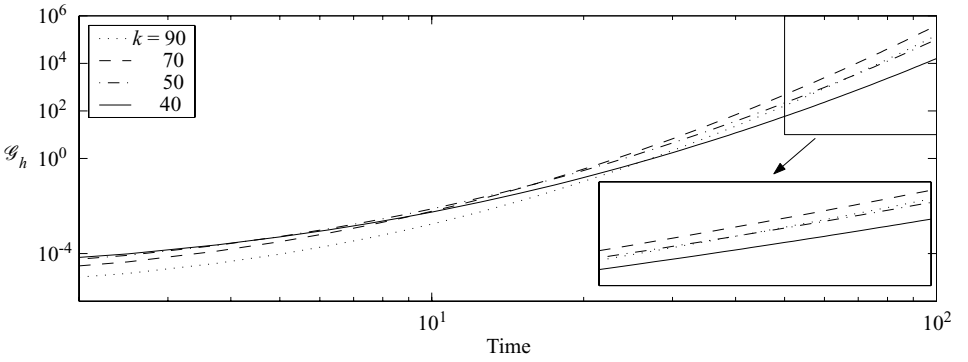

FIGURE 12. The amplification ratio $\mathscr{G}_h$ versus time for various k with the base set of parameters, $R = 10$, $M = 3$.

'dry spot' (although h_0 does not become zero-valued in finite time in the absence of intermolecular forces (Jensen & Grotberg 1992), which have been neglected from the present analysis) immediately downstream of the deposited drop.

4. Stability analysis

As mentioned in the introduction, the spreading process is accompanied by finger formation. It is therefore interesting before presenting our stability results to anticipate how the structural differences to the base state brought about via variation of the parameters associated with the presence of micelles (e.g. R and M) would affect the stability of the system in the light of the fingering mechanism proposed by Warner *et al.* (2004*a*, *b*). These authors established the necessity of having sharp gradients in both h_0 and Γ_0 in the thinned region connecting the drop to the leading front as essential ingredients for instability. They showed that small local perturbations to the film thickness in that region grow, thereby increasing the surface velocity, transporting surfactant away from it. This promotes transverse Marangoni-driven flow from surfactant-rich adjoining regions, which enhances perturbation growth and destabilizes the system, leading to finger formation. Inspection of the h_0 and Γ_0 profiles in figure 5 associated with large M values reveals that $|\Gamma_{0x}|$ is large at the edge of the secondary front. It is expected, therefore, that fingers should form at this point. We turn our attention now to an investigation of the fingering phenomenon, placing particular emphasis on the effect of R and M on the stability characteristics of the system.

4.1. *Transient growth*

As described in § 2.3 we look at the stability of the spreading process to transverse perturbations using a linear stability approach. However, as the base state itself evolves this is done using transient growth analysis with the growth characterized by the growth measures introduced in § 2.3. The base and perturbation equations are solved using the boundary and initial conditions given in § 2.4.

We begin the discussion of the results of our transient growth analysis by showing the amplification ratio, $\mathscr{G}_h$, versus time for various transverse wavenumbers k. It is notable that there is preferred wavember that maximizes growth; for instance in figure 12 we see that $k = 70$ ultimately overtakes the other k values: lower k (cf. $k = 40$

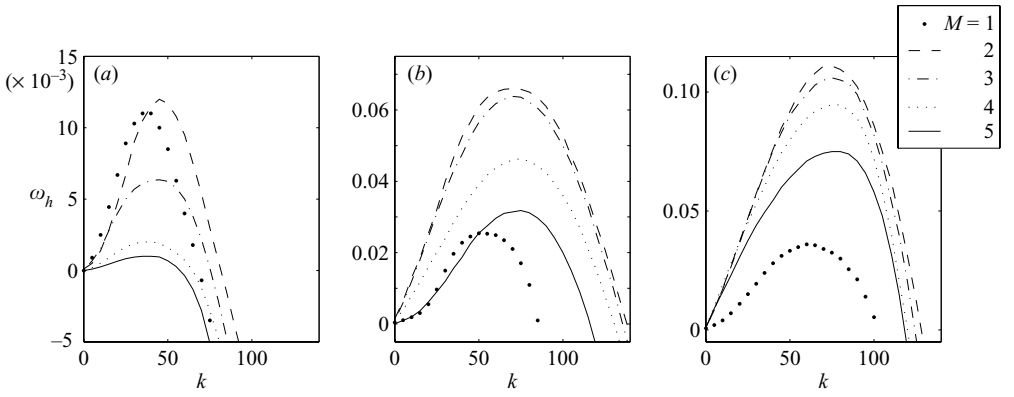

FIGURE 13. 'Dispersion curves' for (*a*) $R = 1$, (*b*) $R = 10$ and (*c*) $R = 100$, using the base case parameter set of figure 4.

in figure 12) are preferred at earlier times, very high k (cf. $k = 90$ in figure 12) are moderated by capillary and hence are not optimal for growth, and so an intermediate wavenumber is ultimately preferred.

It is clearer to visualize trends through numerically generated 'dispersion curves' as in figure 13. Using the growth measures of § 2.3 we extract the asymptotic growth rate ω_h; in practice the values of $\mathscr{G}_h$ at $t = 250$ are used to compute these. We then plot the parameteric dependence of ω_h versus k on the mass M for $R = 1$, $R = 10$ and $R = 100$. The dispersion curves are paraboloidal, exhibiting well-defined 'most-dangerous' and 'cut-off' modes, characterized by wavenumbers k_m and k_c, respectively; the positive values of ω_h for $0 \leqslant k \leqslant k_c$ indicates the presence of an instability. Inspection of figure 13 also reveals that for all values of R examined, $\omega_h(k_m)$ and k_c exhibit a non-monotonic dependence on the mass of surfactant deposited: both $\omega_h(k_m)$ and k_c are maximized for an intermediate value of M, $M = 2$. Beyond this value of M, however, k_m is weakly dependent on M. This indicates that for a given value of R the system is most unstable (and the band of 'unstable' wavenumbers is widest) for concentrations just beyond the CMC; deposition of surfactant solution droplets of higher concentrations leads to a more stable spreading process, characterized by lower $\omega_h(k_m)$ and k_c values. Although one would expect that large concentration gradients, and therefore significant Marangoni stresses, would be more sustainable for larger M values, the spreading is less unstable than for intermediate M for which the height disparity between the protuberance and the downstream minimum is larger than that between the peak of the secondary front and the minimum (see inset of figure 5*a*). In analogy to related interfacial flows involving clean and surfactant-covered thin films driven by body forces and surface stresses (Troian *et al.* 1989*a*; Kataoka & Troian 1997; Eres, Schwartz & Roy 2000; Edmonstone *et al.* 2005), regions which exhibit such height and, therefore, mobility mis-matches are unstable to transverse disturbances; the perturbation growth rate and characteristic wavelength increase with increasing height mis-match.

As also shown in figure 13, increasing R (a preference for the surfactant to be at the interface) is destabilizing leading to a substantial and monotonic increase in both $\omega_h(k_m)$ (approximately a ten-fold increase) and k_m (from $k_m \approx 40$–50 for $R = 1$ through to $k_m \approx 70$–80 for $R = 100$), that is larger growth rates and fingers of shorter wavelength; this is because increasing R promotes the establishment of large concentration gradients and increases the magitude of Marangoni stresses. The cut-off

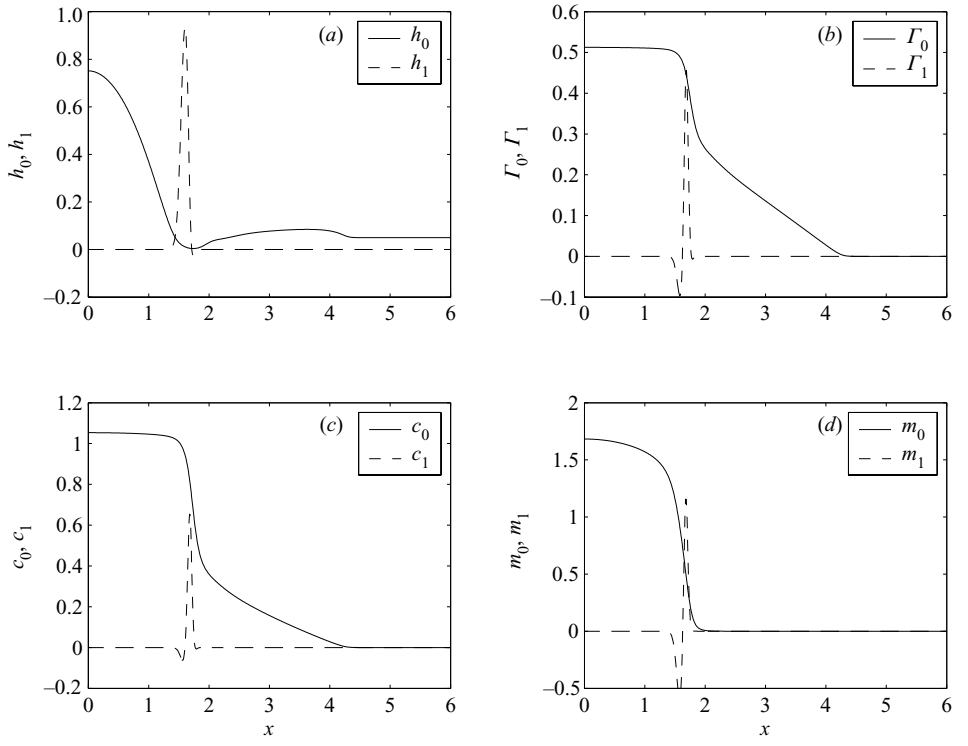

FIGURE 14. Base-state and perturbation profiles for the same parameter set as in figure 6, $k = 40$ and $t = 125$. The amplitudes of the perturbation height are normalized to unity, and the same scaling factor is then applied to the surfactant perturbation.

wavenumber, k_c, on the other hand, also grows monotonically with R for small and large M but appears to saturate with increasing R (and decrease very slightly for large R) for intermediate M values.

Next, we examine the structure of the perturbations in relation to that of the base state in order to determine the region targetted by the instability. We show in figure 14 the base state and perturbation flow profiles for $R = 1$ and the 'base' case parameter set ($\mathscr{C} = 0.001$, $Pe_s = 10^4$, $Pe_b = Pe_m = 100$, $K_s = 1$, $K_b = 1$, $\beta = 1$, $\alpha = 100$, $n = 10$, $M = 3$, $b = 0.05$) at $t = 125$. Here, the amplitude of the perturbation quantities, whose wavenumber coincides with that of the most dangerous mode for these parameters, has been suitably scaled for clarity of presentation. As shown clearly in figure 14, the perturbations in the film thickness and surfactant concentrations target the thinned region connecting the drop and the leading front; this is similar to the result obtained by Warner *et al.* (2004*a*, *b*). Figure 14 also shows that h_1 is 'out of phase' with Γ_1, c_1 and m_1: for a fluid region of increased height the surfactant concentration is lower. The increase in height and lower surfactant leads to an increase in the surface velocity due to the reduction of viscous drag and the increase in the local value of the concentration gradient. This velocity increase leads to faster surfactant transport from this region and, in turn, larger gradients. Transverse Marangoni-driven flow acts to replenish the surfactant deficiency from surfactant-rich adjoining regions, which leads to further thickening of the perturbation in relation to these relatively depressed regions. This, therefore, further destabilizes the system and reinforces the formation of fingers.

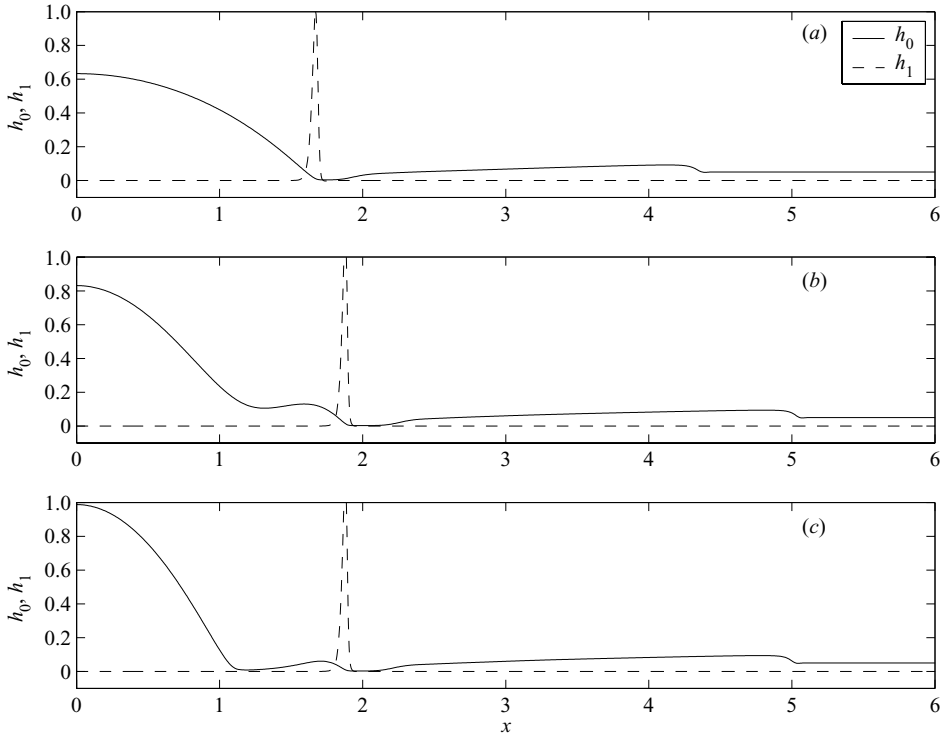

FIGURE 15. Base-state and perturbation thickness profiles for (*a*) $M = 1$, (*b*) $M = 3$, (*c*) $M = 5$. The other parameters are those used in figure 14 except $R = 100$ with profiles shown at $t = 125$. Here, the amplitude of h_1 was normalized to unity in each panel, and the same scaling factor is then applied to the surfactant perturbation.

The results presented in § 3 have shown that, for certain parameter values, the base-state thickness profiles exhibit a qualitatively different feature from that seen in previous studies: the development of a distinct 'protuberance', or a 'secondary' front, between the drop and leading front. Clearly, this feature arises for various combinations of parameters. Rather than conduct an exhaustive parameteric study of the effect of all parameters on the system stability and disturbance structure, we concentrate below on the stability of three qualitatively different base-state thickness profiles obtained by fixing $R = 100$ and varying M (see figure 15): a h_0 profile with no secondary front ($M = 1$), another with a pronounced protuberance but with a single thinned region ($M = 3$) and yet another with a secondary front straddling two thinned regions ($M = 5$) located upstream of the leading front and immediately downstream of the drop.

In figure 15, we show scaled h_1 profiles (with $k = 40$) superimposed upon h_0 in order to determine whether or not the presence of the secondary front affects the structure of the instability. As shown in figure 15, the thinning region connecting the drop (for $M = 1$) or the leading edge of the protuberance and secondary front (for $M = 3$ and $M = 5$, respectively) are vulnerable to transverse perturbations. This is as expected following our examination of the base-state profiles in § 3 (see in particular figure 5*a* (inset) and figure 6) and our discussion above regarding the existence of possible connections with instabilites in related driven thin film flows. In fact, the structural similarity between the protuberance shown for $M = 3$ in figure 5, the fact

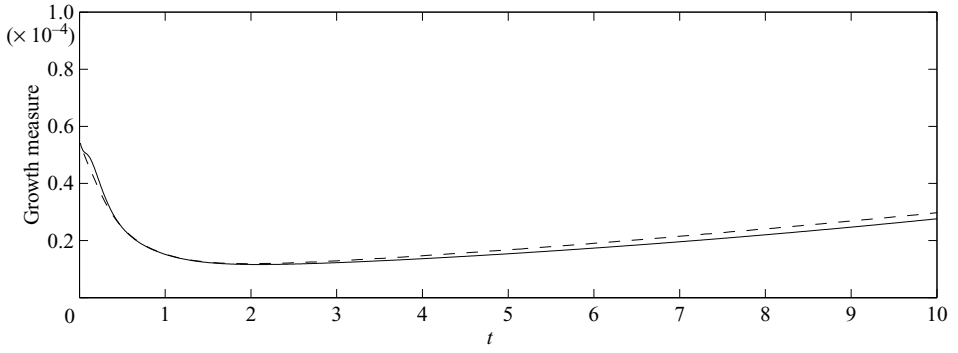

FIGURE 16. A comparison of the transient growth analysis predictions (solid line) and those of the ADI method (dashed line) for $M = 5$, $R = 100$, $b = 0.1$ and $k = 20$; the rest of the parameters are the same as in figure 4. Here, the 'growth measure' is given by (2.52).

that an essentially constant Γ_{0_x} exists over the leading edge of this feature and the fact that it is unstable, suggest a close analogy with the thermally driven thin film problem (Kataoka & Troian 1997) and that involving flow down an incline of a surfactant-covered film (Edmonstone *et al.* 2005). In both of these flows, the surface stress is constant at the leading edge of the advancing ridge, which exhibits fingering. The other thinning region, located downstream of the drop for the largest M value used, appears to be stable. This may be because there exists a pathway to convect perturbations downstream from the thinning region nearest the drop so that they become 'pinned' at the downsloping edge of the secondary front where they can undergo substantial amplification.

Although we have focused on the effect of varying M and R on the stability characteristics, it is, nevertheless, possible to anticipate the effect of n, Pe, $Pe_{b,m}$, b and α on the stability of the spreading process. Inspection of figure 11 reveals that increasing n, Pe, $Pe_{b,m}$ and α, and decreasing b, which give rise to more pronounced secondary fronts, is expected to lead to more unstable spreading. We turn our attention now to the nonlinear stability of the system.

4.2. *Two-dimensional numerical simulations*

In order to complement the results of the transient growth analysis (TGA), which allows the examination of the linear stability of the system only, we have also conducted transient numerical simulations of the fully nonlinear two-dimensional evolution equations (2.17)–(2.20); the objective here is to explore the stability of the flow in the nonlinear regime.

Equations (2.17)–(2.20) are solved using the ADI scheme briefly described in § 2. We have ensured that these nonlinear simulations, in the absence of perturbations, reproduce the base states previously obtained. We have also ensured that, starting from small periodic disturbances of known wavenumber, k, to a base state, the predictions of the ADI procedure are in excellent agreement with those of the TGA; such a cross-validation study is illustrated in figure 16. This inspires confidence not only in the reliability and accuracy of the ADI procedure but also in the TGA results.

Using the validated ADI method we have carried out 'numerical experiments' by applying initial pseudo-random perturbations, taken from a uniform distribution with amplitude $[-10^{-2} : 10^{-2}]$, in $0 < x < 2$. The parameter values used to generate

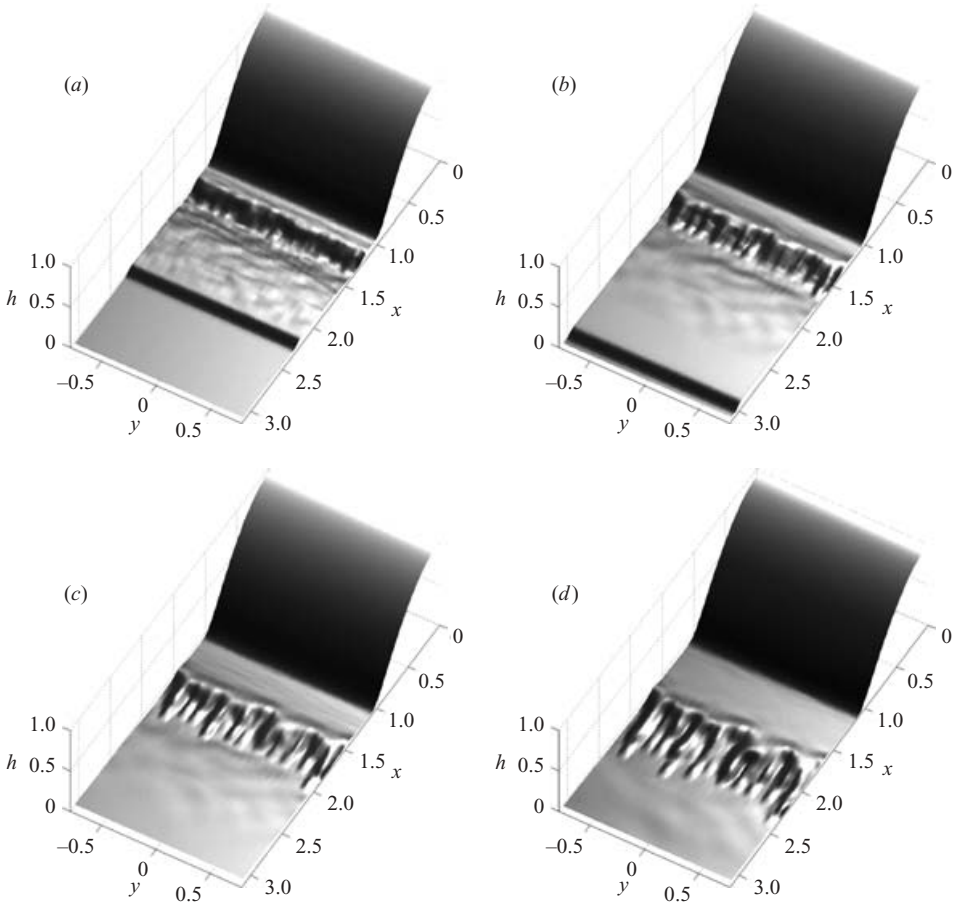

FIGURE 17. The evolution of the film thickness h showing the finger development along the secondary front for $M = 5$, $R = 100$ and the same remaining parameters as in figure 5. (*a*) $t = 10$, (*b*) $t = 25$, (*c*) $t = 50$, (*d*) $t = 100$.

the results presented in this section are $\mathscr{C} = 0.001$, $Pe_s = 10^4$, $Pe_b = Pe_m = 100$, $K_s = 1$, $K_b = 1$, $\beta = 1$, $\alpha = 100$, $n = 10$, $b = 0.05$ and the evolution was then followed to $t = 100$. The film height evolution is shown in figure 17 with $M = 5$ and $R = 100$. It is clear upon inspection of figure 17 that the initially noisy disturbances have organized themselves into coherent structures which appear to target the region between the drop and the leading front preferentially, where the 'secondary' front develops, in agreement with the TGA predictions; remnants of these disturbances are still apparent as surface ripples between this front and the leading front at $t = 10$, which decay at later times. As the secondary front begins to separate from the drop, and another thinning region develops upstream of it, the coherent structures assume the shape of fingering patterns, which, at $t = 100$, resemble those shown in figure 1(*c*); the leading front has propagated far ahead and out of our main region of interest. In contrast to the experimental results of Lee *et al.* (personal communication, 2005) shown in figure 1(*c*), the thinning region immediately upstream of the fingering secondary front is stable. We posit, however, that this region may have become unstable in the presence of intermolecular interactions (such as van der Waals forces): the ramified fingering

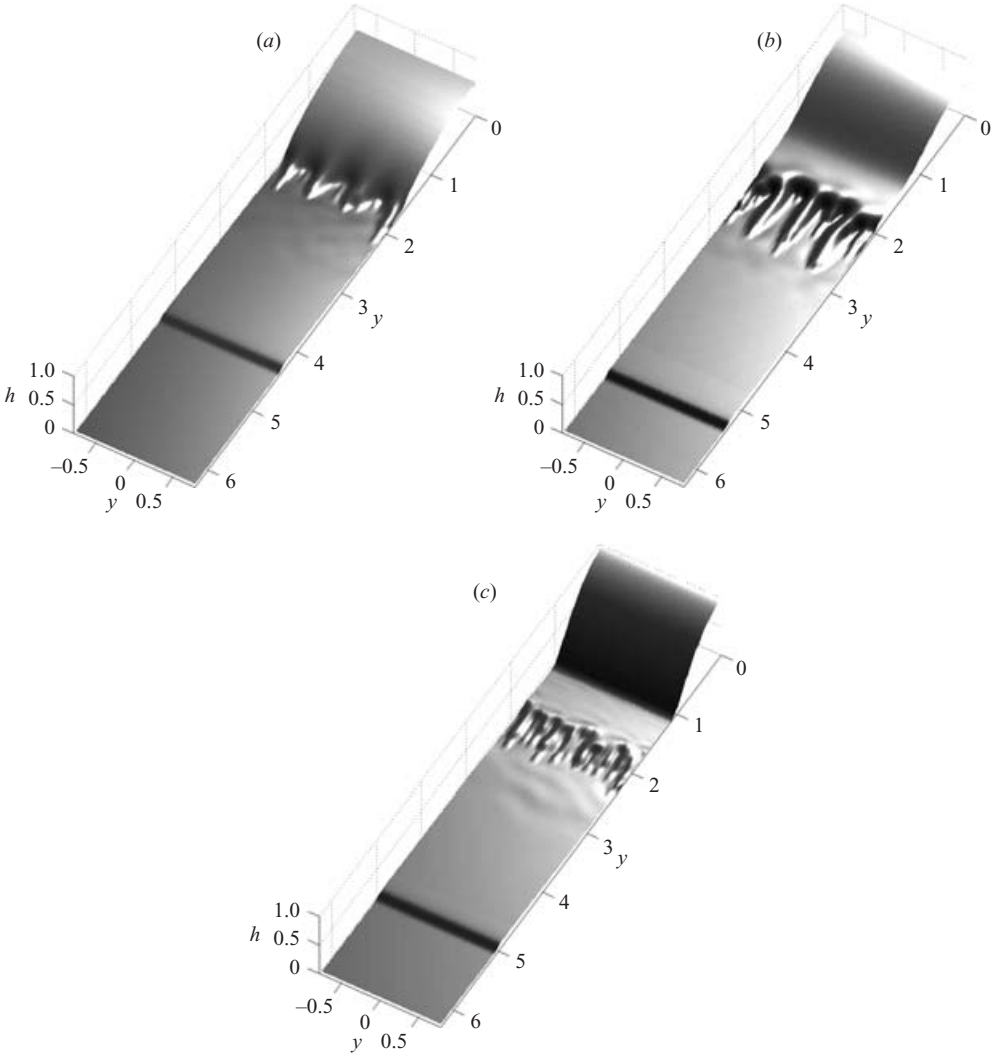

FIGURE 18. The height profiles at $t = 100$ for varying mass (*a*) $M = 1$, (*b*) $M = 3$, (*c*) $M = 5$ and $R = 100$. The rest of the parameters are unchanged from figure 17.

streamlets shown in figure 1(*c*) are structurally rather different from the fingering patterns exhibited by the secondary front, which, in turn, suggests that their origin may also be different.

Using the ADI method, we have also examined the effect of varying the mass of deposited surfactant, M, with the rest of the parameters fixed, on the nonlinear stability of the spreading process. This may be interpreted as being the equivalent of keeping the volume of the deposited drop constant while increasing the concentration of the surfactant solution. In figure 18, we show surface plots of the film thickness for $M = 1, 3, 5$, for relatively long times, $t = 100$. As is clearly shown in this figure, the increase in surfactant mass ($M = 1 \rightarrow M = 3$) acts to destabilize the system, leading to larger growth rates and fingers of shorter wavelength; this is in agreement with the discussion of the TGA results in § 4.1. It is also worthy of mention that the fingering

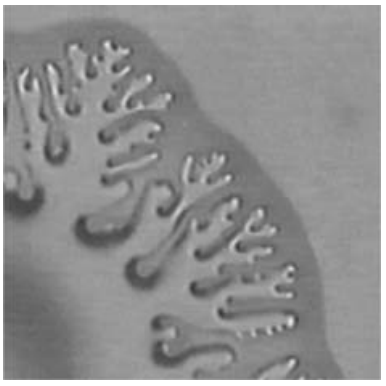

FIGURE 19. An evolving droplet of $C_{12}E_{10}$ at 0.5 CMC spreading on a 60 nm EG film showing branching fingers, taken from Hamraoui *et al.* (2004).

instability occurs in the nonlinear regime for the $M = 3$ case despite the absence of a pronounced thickness minimum between the drop and the leading front, which is in qualitative agreement with the results of Hamraoui *et al.* (2004) shown in figure 1(*b*). That is, the instability appears to target the protuberance between the drop and leading front. We have also included the film thickness surface plot associated with $M = 5$ and $t = 100$ discussed above in figure 18 to facilitate comparisons with the $M = 1$ and $M = 3$ cases. It is clear that increasing M beyond $M = 3$ for this set of parameters renders the spreading less unstable with less pronounced fingering patterns that target the secondary front.

Finally, yet another fingering behaviour appears for some parameter values in experiments, as shown in figure 19, where large fingers emerge from the droplet. Initially, these are a single finger, but these then tip-split repeatedly to grow a tree-like structure. Each finger has a distinct capillary ridge at its tip and both the droplet and fingers appear to be at the same, or very similar, height. We have attempted to reproduce numerically certain details of this fingering phenomenon that are observed experimentally. In particular, we have focused on the tip-splitting events, which are clearly shown to occur in figure 19, following the protrusion of a 'primary' finger from the main spreading drop. The initial conditions we use are those given by (2.50) with the height set such that $A = 1$ and $f(x, y) = 1 + b$ in $y^2 + (x - 2)/2 < 0$ (a parabolic non-trivial geometric perturbation to the drop) and with the surfactant at Γ_o, c_o, m_o within the extruded finger. In figure 20, we show the evolution of this highly localized disturbance to the drop leading edge. As is clearly shown in this figure, the disturbance undergoes a secondary instability that manifests itself in the form of wiggles at $t = 10$ which are particularly prominent at the disturbance leading edge in the $y = 0$ plane; this is as expected since the wiggles in this region grow rapidly under the action of the largest concentration gradient which is in the x-direction. These wiggles become more pronounced with increasing time, leading to the formation of digitated structures that emanate from the initial protrusion. Close inspection of the structures shown at $t = 225$ in figure 20, which bear great resemblence to those shown in figure 19, reveals that the tip of the finger in the $y = 0$ plane has split into two smaller fingers and, as a result, has been 'shielded' slightly by the two slender adjoining fingers, which appear to spread more rapidly. The outermost, broader fingers also appear to have shielded the structures nearest the drop which have not developed into elongated fingers. The

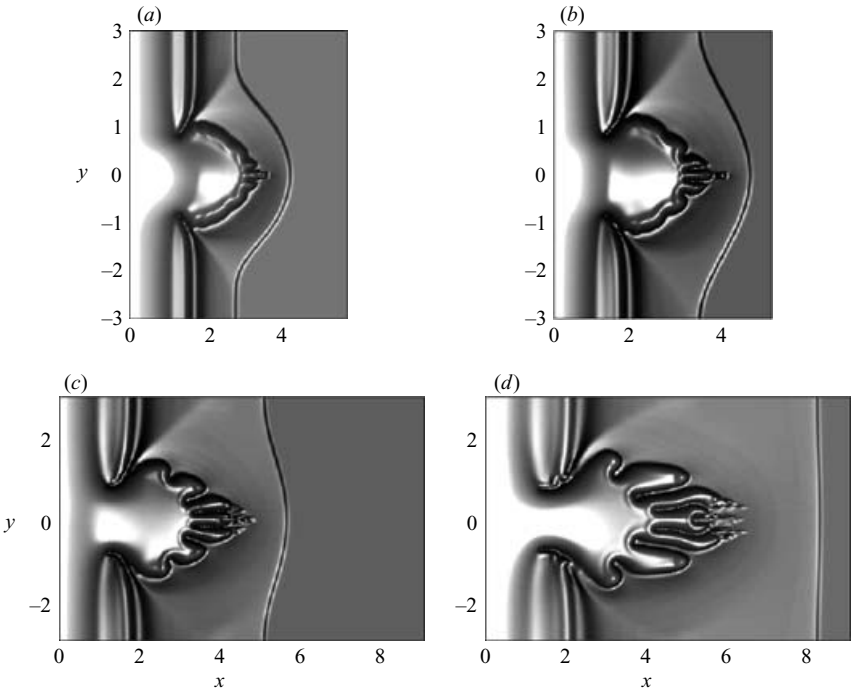

FIGURE 20. The evolution and subsequent tip-splitting of a 'primary' finger protruding from the edge of a drop for the 'base' set of parameters, but with $R = 100$ and $C = 10^{-4}$. The initial conditions are described in the main text. (*a*) $t = 10$, (*b*) $t = 25$, (*c*) $t = 75$, (*d*) $t = 225$.

fingers have developed notable capillary ridges at their tips which are similar to those seen in the experiments; the fingers are also similar in height to that of the main droplet. Also notable in the simulations is the absence of a pronounced minimum.

The application of this localized disturbance to the edge of the drop has therefore resulted in the formation of three generations of fingers and the preferential 'channelling' of the liquid from the drop into these fingers: as shown in figure 20, the drop and the fingers leading edges have spread approximately 0.25 and 3.5 dimensionless units in the x-direction, respectively.

5. Conclusions

The work presented in this paper extends the previous studies of Warner *et al.* (2004*a*, *b*) to cover cases in which droplets of surfactant solution spread on very thin liquid layers at high concentrations, which are typical of experimental situations. It also represents one of the few attempts in the literature at accounting explicitly for the presence of micellar aggregates and their effect on the dynamic evolution of a free surface through their formation and breakup. In addition to demonstrating better agreement with experimental trends and observations in terms of the surfactant spreading problem, this paper, more generally, provides a useful framework for modelling the large-scale evolution of films, threads and jets laden with surfactant beyond the CMC. Such a framework can be utilized to gain insight into phenomena such as super-spreading (Stoebe *et al.* 1997*a*, *b*); such an investigation is already underway.

We have examined the spreading of surfactant on thin liquid films beyond the critical micelle concentration (CMC) using lubrication theory, and assumed rapid vertical diffusion, to derive a coupled system of evolution equations for the film thickness, surfactant monomer surface and bulk concentrations, and micelle bulk concentration. These highly nonlinear, two-dimensional partial differential equations are parameterized by bulk and surface Péclet numbers, a capillary parameter, sorption kinetics constants, a solubility parameter, the size of the micellar aggregates, the nonlinearity of the surfactant equation of state, the dimensionless thickness of the pre-existing film, the mass of deposited surfactant and a parameter reflecting the affinity of the system to form micelles; here, we have focused on the latter two parameters, M and R, respectively.

Our investigation of the unperturbed spreading profiles has shown that for fixed R, a protuberance emerges from the drop, which, with increasing M, separates to form a 'secondary' front, upstream of the primary advancing front, located at the surfactant leading edge. For the largest values of M examined, the unperturbed thickness profiles exhibit two thinning regions that separate the drop and the secondary front, and the primary and secondary fronts; this is in qualitative agreement with experimental observations for spreading at concentrations larger than the CMC. The results of our transient growth analysis and numerical simulations have revealed that increasing R destabilizes the spreading process monotonically, and that process is most unstable for an intermediate value of M; connections with other interfacial instabilities involving driven thin films have also been established. We have also shown that our numerical simulations can capture shielding and tip-splitting events which have been observed experimentally. Detailed analysis of these events will be the subject of future work.

It is also worthwhile to briefly discuss other micelle disassociation models, such as, say, the Fainerman model: the micelle flux (after suitable non-dimensionalization) is $J_{cm} = -K_b m(1-c)$, i.e. it builds in a cut-off preventing disassociation if the bulk monomer concentration is too high. Numerical simulations using this flux, instead of $J_{cm} = K_b(c^n - m)$, for the one-dimensional base states, also yield the same features, i.e. the secondary front, protuberance, etc., suggesting that the features that we describe are not strongly dependent upon the disassociation model.

B.D.E. is funded by the EPSRC through a Research Studentship. The authors wish to thank Professor Anne-Marie Cazabat and Professor Paul Luckham for kindly providing access to much experimental data, allowing use of images used in figure 1 and figure 19 and for useful scientific discussions. We also thank a referee for helpful and useful comments.

REFERENCES

Afsar-Siddiqui, A. B., Luckham, P. F. & Matar, O. K. 2003*a* The spreading of surfactant solutions on thin liquid films. *Adv. Colloid Interface Sci.* **106**, 183–236.

Afsar-Siddiqui, A. B., Luckham, P. F. & Matar, O. K. 2003*b* Unstable spreading of an anionic surfactant on liquid films. Part I: Sparingly soluble surfactant. *Langmuir* **19**, 696–702.

Afsar-Siddiqui, A. B., Luckham, P. F. & Matar, O. K. 2003*c* Unstable spreading of an anionic surfactant on liquid films. Part II: Highly soluble surfactant. *Langmuir* **19**, 703–708.

Bardon, S., Cachile, M., Cazabat, A. M., Fanton, X. & Villette, S. 1996 Structure and dynamics of liquid films on solid surfaces. *Farad. Disc.* **104**, 307–316.

Breward, C. J. & Howell, P. D. 2004 Straining flow of a micellar surfactant solution. *Eur. J. Appl. Maths* **15**, 511–531.

Cachile, M. & Cazabat, A. M. 1999 Spontaneous spreading of surfactant solutions on hydrophilic surfaces:cnem in ethylene and diethylene glycol. *Langmuir* **15**, 1515–1521.

Cachile, M., Cazabat, A. M., Bardon, S., Valignat, M. P. & Vadenbrouck, F. 1999 Spontaneous spreading of surfactant solutions on hydrophilic surfaces. *Colloids Surf.* A **159**, 47–56.

Cachile, M., Schneemlich, M., Hamraoui, A. & Cazabat, A. M. 2002 Films driven by surface tension gradients. *Adv. Colloid Interface Sci.* **96**, 59–74.

Chang, C.-H. & Frances, E. I. 1995 Adsorption dynamics of surfactants at the air/water interface: a critical review of mathematical models, data, and mechanisms. *Colloids Surf.* A **100**, 1–45.

Darhuber, A. A. & Troian, S. M. 2003 Marangoni driven structures in thin film flows. *Phys. Fluids* **15**, S9.

Edmonstone, B. D. 2005 Dynamics of surfactant-laden thin films. PhD thesis, Imperial College London.

Edmonstone, B. D., Matar, O. K. & Craster, R. V. 2005 Coating of an indined plane in the presence of insoluble surfactant. *J. Colloid Interface Sci.* **287**, 261–272.

Edwards, D. A., Brenner, H. & Wasan, D. T. 1991 *Interfacial Transport Processes and Rheology*. Butterworth-Heinemann.

Eres, M. H., Schwartz, L. W. & Roy, R. V. 2000 Fingering phenomena for driven coating films. *Phys. Fluids* **12**, 1278–1295.

Fischer, B. J., Darhuber, A. A. & Troian, S. M. 2001 Streamlets and branching dynamics in surfactant-driven flows. *Phys. Fluids* **13**, 9.

Fischer, B. J. & Troian, S. M. 2003 Thinning and disturbance growth in liquid films mobilized by continuous surfactant delivery. *Phys. Fluids* **15**, 3837–3845.

Frank, B. & Garoff, S. 1995 Origins of the complex motion of advancing surfactant solutions. *Langmuir* **11**, 87–93.

Gaver III, D. P. & Grotberg, J. B. 1990 The dynamics of a localized surfactant on a thin film. *J. Fluid Mech.* **213**, 127–148.

Hamraoui, A., Cachile, M., Poulard, C. & Cazabat, A. M. 2004 Fingering phenomena during spreading of surfactant solutions. *Colloids Surf.* A **250**, 215–221.

He, S. & Ketterson, J. 1995 Surfactant driven spreading of a liquid on a vertical surface. *Phys. Fluids* **7**, 2640–2647.

Hunter, R. J. 1991 *Foundations of Colloid Science*. Oxford University Press.

Jensen, O. E. & Grotberg, J. B. 1992 Insoluble surfactant spreading on a thin viscous film: shock evolution and film rupture. *J. Fluid Mech.* **240**, 259–288.

Jensen, O. E. & Grotberg, J. B. 1993 The spreading of heat or soluble surfactant along a thin film. *Phys. Fluids* A **5**, 58–68.

Jensen, O. E. & Naire, S. 2006 The spreading and stability of a surfactant-laden drop on a prewetted substrate. *J. Fluid Mech.* **554**, 5–24.

Kataoka, D. E. & Troian, S. M. 1997 A theoretical study of instabilities at the advancing front of thermally driven coating films. *J. Colloid Interface Sci.* **192**, 350–362.

Keast, P. & Muir, P. H. 1991 Algorithm 688 EPDCOL - a more efficient PDECOL code. *ACM Trans. Math. Software* **17**, 153–166.

Liao, Y., Basaran, O. B. & Franses, E. I. 2003 Micellar dissolution and diffusion effects on adsorption dynamics of surfactants. *AIChE J.* **49**, 3229–3240.

Marmur, A. & Lelah, M. D. 1981 The spreading of aqueous surfactant solutions on glass. *Chem. Engng. Commun.* **13**, 133–143.

Matar, O. K. & Troian, S. M. 1999 The development of transient fingering patterns during the spreading of surfactant coated films. *Phys. Fluids* **11**, 3232–3246.

Noskov, B. A. 2002 Kinetics of adsorption from micellar solutions. *Adv. Colloid Interface Sci.* **95**, 237–293.

Sheludko, A. 1967 Thin liquid films. *Adv. Colloid Interface Sci.* **1**, 391–464.

Sincovec, R. F. & Madsen, N. K. 1979 Algorithm 540 PDECOL. *ACM Trans. Math. Software* **5**, 326–351.

Starov, V. M., de Ryck, A. & Vercarde, M. G. 1997 On the spreading of an insoluble surfactant over a thin viscous layer. *J. Colloid Interface Sci.* **90**, 104–113.

Stoebe, T., Lin, Z., Hill, R. M., Ward, M. D. & Davis, H. T. 1997*a* Enhanced spreading of aqueous films containing ethoxylated alcohol surfactants on solid substrates. *Langmuir* **13**, 7270–7275.

Stoebe, T., Lin, Z., Hill, R. M., Ward, M. D. & Davis, H. T. 1997*b* Enhanced spreading of aqueous films containing trisiloxane surfactant on mineral oil. *Langmuir* **13**, 7282–7286.

Troian, S. M., Herbohlzheimer, E. & Safran, S. A. 1990 Model for the fingering instability of spreading surfactant drops. *Phys. Rev. Lett.* **65**, 333–336.

Troian, S. M., Herbolzheimer, E., Safran, S. A. & Joanny, J. F. 1989*a* Fingering instabilities of driven spreading films. *Europhys. Lett.* **10**, 25–30.

Troian, S. M., Wu, X. L. & Safran, S. A. 1989*b* Fingering instability in thin wetting films. *Phys. Rev. Lett* **62**, 1496–1499.

Warner, M. R. E., Craster, R. V. & Matar, O. K. 2002 Unstable van der Waals driven line rupture in Marangoni driven thin viscous films. *Phys. Fluids* **14**, 1642–1654.

Warner, M. R. E., Craster, R. V. & Matar, O. K. 2004*a* Fingering phenomena associated with insoluble surfactant spreading on thin liquid films. *J. Fluid Mech.* **510**, 169–200.

Warner, M. R. E., Craster, R. V. & Matar, O. K. 2004*b* Fingering phenomena created by a soluble surfactant deposition on a thin liquid film. *Phys. Fluids* **16**, 2933–2951.

Witelski, T. P. & Bowen, M. 2003 ADI schemes for higher-order nonlinear diffusion equations. *Appl. Numer. Maths* **45**, 331–351.